Ultrasonic characterization of Ti-5Al-5Mo-5V-3Cr

by

Ruth Sunderman

A thesis submitted to the graduate faculty

in partial fulfillment of the requirements for the degree of

MASTER OF SCIENCE

Major: Materials Science and Engineering

Program of Study Committee:
Peter Collins, Major Professor
Siddhartha Pathak
Ronald Roberts

Iowa State University

Ames, Iowa

2023

NSC-614-5646 10/2023 Unclassified Unlimited Release

DEDICATION

This thesis is dedicated to my parents, my sisters and all the friends who have provided immeasurable love and support throughout my engineering education and career.

Get wisdom, get understanding; do not forget my words or turn away from them.

Proverbs 4:5

TABLE OF CONTENTS

Page

LIST OF FIGURES

LIST OF TABLES

NOMENCLATURE

Ti-5553	Ti-5Al-5Mo-5V-3Cr
NDE	Nondestructive Evaluation
AM	Additive Manufacturing
FFT	Fast Fourier Transform
BW	Backwall
FW	Frontwall
SAW	Surface Acoustic Wave

ACKNOWLEDGMENTS

I would like to thank my committee chair, Dr. Peter Collins, and my committee members, Dr. Pathak and Dr. Roberts for their guidance and support throughout the course of this research. Thank you to the colleagues, the department faculty and staff for making my time at Iowa State University a wonderful experience.

In addition, I would like to thank ATI for supplying the Ti-5553 material used in my study, Trond Forre for encapsulating my samples, and Niraj Atale for collecting nano indentation measurements. Thank you also to Dan Barnard who broadened my knowledge of ultrasonic testing and graciously let me use his ultrasonic testing equipment,

I would like to acknowledge my fellow research group members for training me to use equipment and helping me with my research. In particular, Katie O’Donnell for training me on the Zwick Roell used for hardness and cyclic indentation and writing a highly effective code for acquiring measurements, and Andrew Temple for aiding me in the selection of heat treatments. Finally Maria Quintana-Hernandez for the many and various ways she helped me with my research and reviewing my writing and Thivani Senathiraja for her support throughout my graduate school journey.

I would like to thank Ben Brown for mentoring me throughout my technical fellowship, and Brian Herald for diligently keeping me up to date on KCNSC activities and providing support whenever I needed it.

This work was funded by the Department of Energy’s Kansas City National Security Campus operated by Honeywell.Federal Manufacturing and Technologies, LLC under contract number DE-NA0002839.

ABSTRACT

Metastable β titanium alloys such as Ti-5Al-5Mo-5V-3Cr are of increasing interest due to their excellent corrosion resistance, high strength, and in particular, the ability to manipulate microstructure to a high degree to control the mechanical properties of the material. It is therefore important to consider how this manipulation of mechanical properties will affect the inspection of this material with ultrasonic testing both for the purposes of flaw detection and material characterization. The connection between material properties and ultrasonic characterization techniques will be discussed and then dissected in the context of Ti-5553. This metastable alloy was shown to exhibit remarkable variation in microstructure as well as ultrasonic velocity and attenuation demonstrating these techniques as potential candidates for characterizing Ti-5553 and Ti-5553 as a good candidate for aiding in future studies aimed at learning more about the role of secondary phases in ultrasonic wave propagation.

CHAPTER 1. MOTIVATION AND BACKGROUND

MOTIVATION

Ultrasonic testing is a critical inspection method in nondestructive evaluation (NDE). It is frequently required for flaw detection, but it can be used for characterization as well. This field has been well studied since the 19th century with Lord Rayleigh's two volume publication of *Theory of Sound* in 1876 and 1877 [1]. The field evolved after the famous sinking of the Titanic to use sound in the form of sonar which was quickly adopted for use by submarines, and it was adapted for use as means of flaw detection in the 1940's in support of the war effort [2]. The decades between the end of World War II and today have seen much advancement in the research and industrial adoption of ultrasonic testing to an extent that it may be perceived that the fundamentals of ultrasonic wave behavior are well understood. In this thesis, it may be found that advances in metallurgy can highlight some assumptions that have seeped into the industrial application of ultrasonic testing that may not be adequately accounted for without effective collaboration between the academic and industrial worlds of both materials science and NDE. This collaboration is particularly important for the development of inspection techniques of additive manufacturing (AM) [3].

An example of assumptions in ultrasonic testing that can be problematic when applied too broadly to newer alloys is presented by Professor Washer from the University of Missouri in his study of ultrasonic testing for bridges in 2021 [4]. His lab group has shown that velocity differences of 2.5% or greater between structural steel alloys and their corresponding calibration samples can effectively invalidate a nondestructive test [4]. Alarmingly, the amount of velocity variation expected in a material is not a commonly known when developing inspection procedures or models. The work presented in this thesis will demonstrate the amount of acoustic variation in a particular metastable β titanium alloy Ti-5Al-5Mo-5V-3Cr. The amount of acoustic variation demonstrated in this alloy can be interpreted positively as an opportunity for identification of metallurgical properties using relatively easy to implement tests (because the ultrasonic test equipment is not unusual for a laboratory environment). Alternatively, the results of this research can be thought of as a caution for applying typical ultrasonic testing procedures to β-stabilized titanium alloys without first understanding the inherent processing variability.

Ti-6Al-4V has been the dominant titanium alloy used and inspected to date, but additional alloys such as the β-stabilized alloy Ti-5Al-5Mo-5V-3Cr which can exhibit wide variation in microstructure and resultant properties through heat treatments are gaining in popularity. A study was conducted to create a collection of nearly identical samples that were altered with heat treatments to precipitate the widest possible range of microstructures and then tested with ultrasonic velocity and attenuation tests to see how this variation in microstructure corresponds to a variation in acoustic material properties.

BACKGROUND

To study the ultrasonic characterization of Ti-5553, it is necessary to have a metallurgical understanding of Ti-5553: what types of microstructures exist, how to modify them, and the connection between microstructure and properties. It is then important to have an understanding of the measurable properties of a propagating ultrasonic wave that can connect to microstructural variation. Later sections will discuss how the microstructural, mechanical and ultrasonic measurements fit (or don't fit) with the understanding of the relationship between ultrasonic waves and microstructure.

Ti 5Al-5Mo-5V-3Cr

Titanium alloys have been referred to as the "prima donna" of metals because of excellent corrosion resistance at low temperatures but high reactivity at temperatures above 500°

C including oxygen and nitrogen absorption, scale formation, dissolving of refractory materials used for casting, and even combustion[5]. Ti has a high strength to weight ratio, but the low thermal conductivity creates machining challenges requiring coolant to prevent excessive tool wear and combustion risks. Ti is an abundant element but refinement by the Kroll and Cambridge processes is expensive. Ti alloys are of interest for additive manufacturing (AM) because net shape Ti parts waste less of this expensive resource and reduce the need for welding, machining and casting. In addition, AM can accommodate an inert atmosphere because of automation.

Ti alloys exhibit the body-centered cubic (BCC) β phase at elevated temperatures and a variant of the hexagonal close-packed (HCP) α, α+β, or β phase at room temperature based on the alloying elements that either raise or lower the β solvus [6]. Alloys that are α-stabilized can form a single α phase at room temperature, α+β alloys form both phases at room temperature, and β-stabilized alloys can form purely the β phase or a somewhat customizable amount and type of α phase with heat treatments or thermomechanical processing [7–9]. These alloying elements and the corresponding stabilization effects are categorized in Figure 1.1.

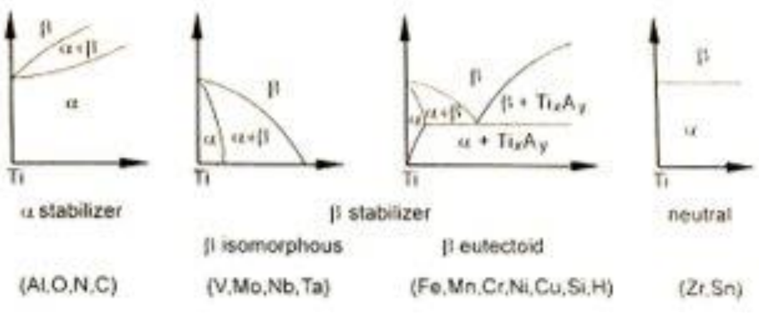

Figure 1.1. List of alloying elements, categorization by stabilization type, and schematic representations of resulting phase diagrams[6].

Ti-5553 is a β-stabilized alloy with Mo, V, Cr, and 0.5% of Fe β-stabilizing elements and Al as an α stabilizer. Ti alloys can be classified based on stabilization according to the Moequivalence (Mo-Eq) scale [10]. Ti-5553 is considered to be a metastable β alloy, but the Mo-Eq places Ti-5553 on the borderline between near-β and metastable β as can be seen in Figure 1.2. This means that Ti-5553 can form combinations of β, α, isothermal ω, and athermal ω depending on cooling rate. Both ω phases have a hexagonal crystal structure. The presence of the athermal ω phase can be verified with electron diffraction and is assumed to always be present in the single β phase microstructure [7,11]. The isothermal ω phase precipitates on aging at temperatures below 500° C [10] and is typically avoided because of an associated embrittling effect. However, it has been demonstrated that the isothermal ω phase can be used to influence α precipitation [12]. Aging at a temperature between 350-400° C to form isothermal ω and then increasing the temperature to the range of 500-600° C for fine α phase will cause intragranular α precipitation at prior ω sites instead of the typical α precipitation from β grain boundaries [12,13]. The β solvus is in the range of 850-880° C [7].

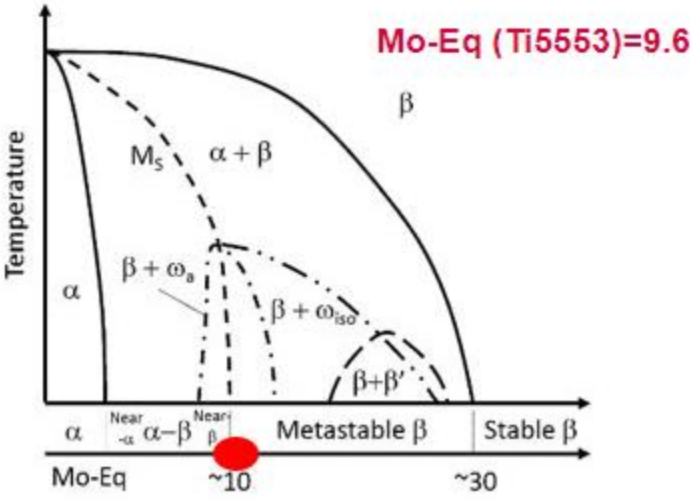

$$\mathbf{Mo - Eq} \\ \mathbf{= Mo + 0.67V + 0.44W + 0.28Nb + 0.22Ta + 2.9Fe} \\ \mathbf{+ 1.6Cr - 1.0Al}\ \ (\mathrm{wt\%})$$

Figure 1.2. Schematic representation of Mo-Eq stabilization and corresponding phases at room temperature [10].

This study focuses on the role of the α phase in performance and the effect on ultrasonic response. The α phase begins to form at approximately 500° C up to approximately 750”C at aging times of approximately 3 hours as can be seen in the Time Temperature Transformation (TTT) diagram created by Cotton et al [7] in Figure 1.3. At lower temperatures, fine α platelets form. The α-lath thickness increases to form coarse α at elevated temperatures. Since the α phase is HCP, it causes an increase in strength from the pure β phase, but there are various mechanisms that account for this change. The coarse α laths that form at elevated temperatures have less of an impact on increases in strength because the coarse laths are easily deformable while the fine laths act as hard indeformable particles [6]. Inter-lath spacing and total phase fraction have been shown to have the greatest impact on yield strength according to the work conducted by Temple [8]. Lath thickness is also a useful metric for use in comparisons to literature and discussions of ultrasonic response. The effects of α type on mechanical performance is illustrated by the series of stress strain curves from AM Ti-5553 published by Carlton [14] in Figure 1.4. Fine α is precipitated between approximately 400 and 600°C and the presence of this phase is evidenced by the distinct increase in strength and decrease in ductility at 400, 500 and 600°C. The curve for 400°C could potentially be attributed to fine α or ω since 400°C is at the lower end of the range of temperatures for forming fine α.

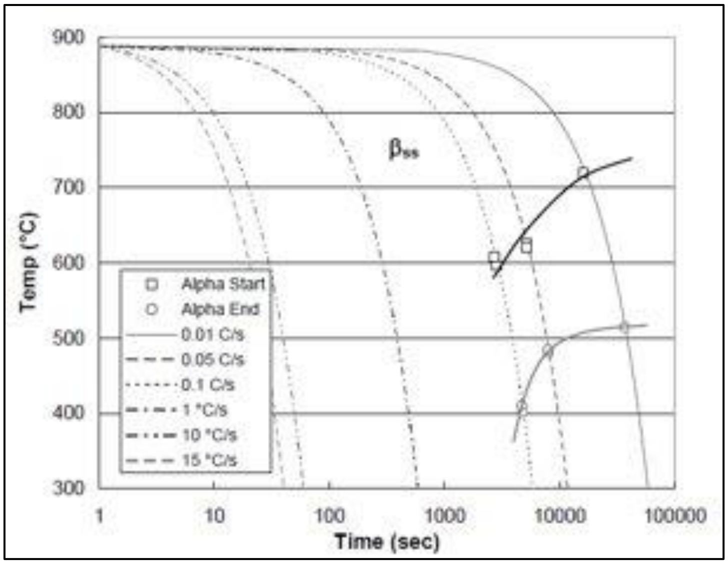

Figure 1.3: TTT curve of Ti-5553 [7].

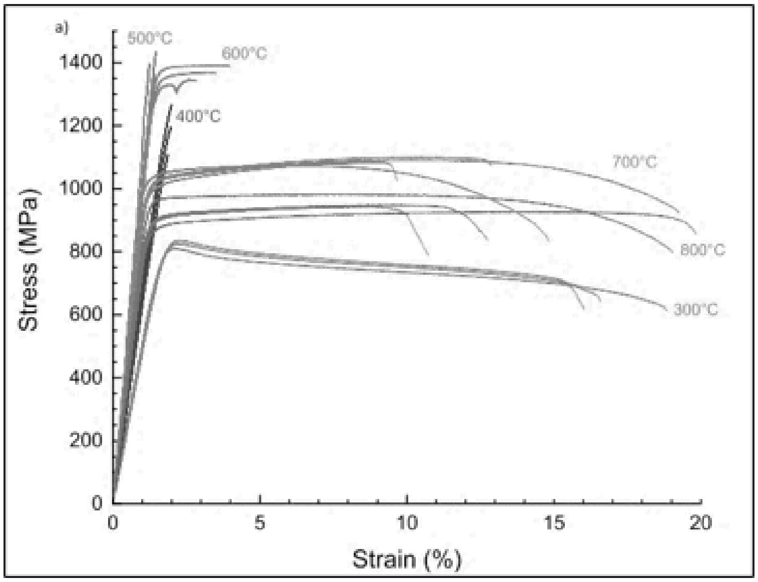

Figure 1.4. Stress strain curves representing AM Ti-5553 15 mm x 60 mm plates. Each sample was stress relieved prior to the study and then held at the respective temperature prior to air cooling [14].

This introduction to the physical metallurgy, including phase transformations and phase stability of Ti-5553 is intended to introduce the alloy and is not intended to be exhaustive. More robust background on this alloy can be found in the theses of Temple [8], Foltz [15], Welk [16], and Clement [9] as well as in the peer reviewed literature [10,12,17].

Ultrasonic Characterization

Ultrasonic testing (UT) is one of the core tools used in the field of Nondestructive Evaluation (NDE). UT is commonly used for flaw detection, but it can also be used as a materials characterization tool. This section will provide a discussion of how ultrasonic waves interact with materials and the material properties that can be extracted from ultrasonic velocity and attenuation.

Ultrasonic Wave Behavior

Ultrasound travels through materials as a mechanical wave that perturbs a medium at an atomic level. Waves will travel at a constant, media-dependent speed until they attenuate or interact with a boundary between media. In general, the greater the distance between atoms, the slower the wave speed will be so gases tend to be poor conductors of ultrasonic waves and solids good conductors. At boundaries, the wave will perform at least one of the following interactions: transmission, reflection, and refraction. In addition, boundary interaction may cause the wave to change speed, convert to a new wave mode or reflect in a way that causes the wave to scatter and lose energy. Examples of boundaries could include transitions among states of matter, transitions from one solid material to another or even transitions between grains. The greater the difference in acoustic velocity and impedance, the less transmission and greater reflection and attenuation will occur. In practice, ultrasound is most commonly generated with a transducer containing a piezoelectric crystal that typically requires some sort of liquid couplant to increase the sound energy imparted to the test object. When the sound wave reaches the bottom of the test object, the sound wave can then be coupled into a second receiving transducer, or the boundary between the bottom of the test object and air can be utilized to reflect the ultrasonic wave back to transmitting transducer for reception. Lasers can also be used for ultrasonic generation and detection. Super heating of material surfaces will also generate an initial, nonlinear ultrasonic pulse which can then be detected as a perturbation in the material surface using a second laser or a coupled transducer (Figure 1.5).

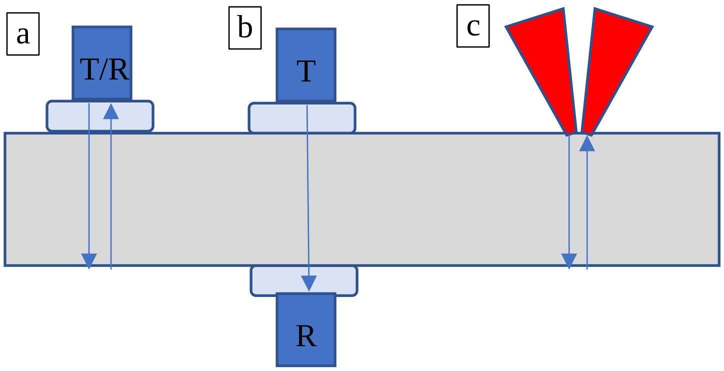

Figure 1.5: (a) A transmitting and receiving transducer is used to couple an ultrasonic wave into a test object and then receives the reflected wave. (b) Separate transducers transmit and receive an ultrasonic wave coupled into and out of the test object. (c) Laser beams are used to generate and detect an ultrasonic wave directly on the surface of a test object.

Ultrasonic wave behavior has been modeled extensively. Some books exist that lay out the foundations of a mathematical understanding of ultrasonic wave behavior and material interactions[18–20]. The most commonly identified version of the wave equation is for the example of a longitudinal wave in a thin rod as can be seen in Equation 1[19]:

$$E\frac{\partial^2 u}{\partial x^2} = \rho\frac{\partial^2 u}{\partial t^2} \qquad \text{Eq. 1}$$

Here, E is Young's Modulus, ρ is the mass density, t is time and u is displacement. This equation is valid in the case of isotropic[1] materials. Using Equation 1, the harmonic wave solution in Equation 2 can be used to describe wave propagation where the coefficient A describes the amplitude, ω is the angular frequency, and k is the wave number[19].

$$u_x = Ae^{i\omega t - ikx} \qquad \text{Eq. 2}$$

In addition, the D'Alembert solution in Equation 3 can be used to describe wave motion as well and is especially useful when considering wave interactions at boundaries in a medium or other disturbances to the wave motion. Here f and g are arbitrary forcing functions that would be determined by the initial conditions of the problem.[19]

$$u(x,t) = f(x - c_0 t) + g(x + c_0 t), \text{ where } c_0 = \sqrt{\frac{E}{\rho}} \qquad \text{Eq. 3}$$

When considering the use of ultrasound for material characterization, the two ultrasonic measurements of primary consideration are the velocity of an ultrasonic wave and its attenuation. According to Ensminger, in order to determine the elastic properties of a material, velocity is the measurement to consider.[18] Attenuation cannot be described quite as distinctly. Ensminger simply states that the "mechanisms producing losses of energy control attenuation" [18]. Both velocity and attenuation will be described in the proceeding sections as well as a more detailed description of the material properties associated with each.

---

[1] In the case of anisotropic materials, the appropriate, material-dependent elastic stiffness tensor must be used to describe wave propagation using $\sigma_{ij}(x,t) = \sum_{k,l=1}^{3} c_{ijkl}(x) \frac{\partial}{\partial x_l} u_k(x,t)$. The invocation of anisotropic behavior through the elastic stiffness tensor C_{ij} will lead, necessarily, to different formula for equations 4-7, and likely others throughout this thesis.

Ultrasonic Velocity and Modulus

The isotropic elastic properties calculable using ultrasonic velocity are the elastic, shear and bulk moduli and Poisson’s ratio. These relationships are well known and listed in Equations 4-7 where v_L is the longitudinal velocity, v_S is the shear velocity, and ρ is density.[21]

$$E = \frac{\rho v_T^2 (3v_L^2 - 4v_S^2)}{(v_L^2 - v_S^2)} \qquad \text{Eq. 4}$$

$$G = \rho v_S^2 \qquad \text{Eq. 5}$$

$$B = \rho \left(v_L^2 - \frac{4}{3} v_S^2 \right) \qquad \text{Eq. 6}$$

$$\nu = \frac{(v_L^2 - 2v_S^2)}{2(v_L^2 - v_S^2)} \qquad \text{Eq. 7}$$

A third wave mode called a Rayleigh wave (also referred to as surface acoustic waves or SAWs) is also relevant to this research and can be related to longitudinal and shear waves using Equation 8, where $\eta = \frac{v_R}{v_S}$ and $\nu = \frac{v_S}{v_L}$.[18]

$$\eta^6 - 8\eta^4 + 8(3 - 2\nu^2)\eta^2 - 16(1 - \nu^2) = 0 \qquad \text{Eq. 8}$$

Longitudinal and shear velocity measurements are fairly routine and are some of the first measurements a practitioner of ultrasonic testing learns how to make. All that is required to make this measurement is an oscilloscope or a flaw detector and a physical measurement of sample thickness. In industry, tables are frequently used that list a single velocity for a class of materials [22]. For example, the velocity of titanium is commonly known to be 6100 m/s. In practice, these numbers are used as a reference for tests such as measuring material thickness. There are also examples of velocity measurements being used to make more precise measurements of material properties such as the quantity of graphite in cast iron [23] and estimate average grain size in AISI type 316 stainless steels.[24]

In a polycrystalline material, velocity is known to vary from grain to grain because it is dependent on crystallographic orientation and texture, however velocity is typically only able to be measured of a polycrystalline aggregate because single crystal metals are relatively uncommon in applications requiring NDE. Previous work has been performed to quantify texture using ultrasonic velocity used bulk SAW velocity measurements to create pole figures comparable to figures generated using x-ray diffraction.[25,26] Spatially Resolved Acoustic Spectroscopy (SRAS) is a new technology which uses measurements of grain velocity to determine crystallographic orientation and thus is capable of mapping the texture of relatively large sample sizes compared to Electron Backscatter Diffraction (EBSD) [27]. EBSD is more commonly used for crystallographic orientation and material texture but over small sample sizes with a higher degree of surface preparation required. Comparing SRAS to bulk velocity measurements will provide the opportunity to compare local and bulk velocity measurements and determine how the velocity distribution compares to bulk measurements.

Ultrasonic Attenuation and Microstructure

Ultrasonic attenuation can have many causes such as frictional losses, micro eddy currents, heat conduction, motions of atoms caused by stress, dislocations and, most importantly, grain boundary interactions [18]. The interaction with grain boundaries is considered to be the most important cause for attenuation, and it can also provide a convenient method for measuring grain size [28]. These lists of attenuation sources exclude defects such as pores and inclusions, but defects also have a dramatic effect on wave scattering.

Attenuation is one of the primary limiting factors when determining whether a component may be inspected with ultrasonic testing, but attenuation measurements can also be used as a characterization tool to indicate grain size. There are some well-established models for grain boundary scattering [29–32], but they are most easily applied to single phase, crystalline systems. Work has been done to extend these models to polycrystalline, non-cubic, or texturing effects on attenuation [33–37], but they inherently tend to assume uniformity in secondary phases or single phase material. In a study by Zhang et al, single-phase copper was selected to measure with the criteria that it is defect free, manufactured with uniform grain structure and is likely to exhibit grain boundary scattering over other sources of attenuation [38]. In this study, powder metallurgy samples were compared to wrought samples to determine if the existing models for attenuation due to grain scattering really fully captured this phenomenon. Both types of samples had comparable grain sizes but differences in attenuation indicating that the attenuation models do not fully describe this phenomenon. In this thesis, a proof of concept investigation of β-stabilized Ti-5553 was made because this particular alloy can be quenched to form pure β phase, or tailorable types and quantities of α phase permitting the effects of type, phase fraction and lath thickness of α to be directly observed.

Measuring attenuation and velocity of β-stabilized titanium alloys is not entirely new. Viswanath attempts to measure the phase fraction of the α phase in the β stabilized alloy Ti-10V-4.5Fe-1.5Al. In this study samples are β solutionized for 1 hour followed by 1 hour heat treatments at 50° C intervals ranging from 550°-900° C before water quenching. A correlation is shown between phase fraction of α, velocity and attenuation, but there is no discussion of the differences between coarse α and fine α [39]. Since these aging times are relatively short and all the same duration, more of the fine α phase is able to nucleate than the coarse α phase which barely nucleates at all. In this study of Ti-5553, samples were given a uniform β solutionizing treatment followed by adequately long aging times at temperatures demonstrated to nucleate specific α phases.

In this study of attenuation due to α content, it is prudent to consider not just the phase fraction of α, but also the importance of the size of α relative to wavelength as well as the effect of α on the scattering of ultrasound from β grain boundaries. Stanke and Kino's model for attenuation creates three categories for the relationship between grain size, anisotropy, and wavelength for the purposes of modeling attenuation due to grain boundary scattering [30]. These regions are given by equations 9-11 where x is the wave number multiplied by grain diameter(d) or $\frac{2\pi d}{\lambda}$ where λ is the wavelength and ϵ is an inhomogeneity factor. In the Rayleigh region, the wavelength of the ultrasonic wave is larger than the grain size. Since fine α is typically on the order of nanometers, fine α laths considered as a grain would fit in the Rayleigh region and should theoretically have little impact on attenuation.

$$Rayleigh\ zone = x < 1 \qquad \text{Eq. 9}$$

$$Stochastic\ zone = 1 < x < \frac{1}{\epsilon} \qquad \text{Eq. 10}$$

$$Geometric\ zone = \frac{1}{\epsilon} < x \qquad \text{Eq. 11}$$

In the stochastic zone, the grain size could be larger than the wavelength with a low degree of inhomogeneity. The wavelength of an ultrasonic wave is the material velocity divided by the frequency of the wave. The central frequencies of the transducers used to measure velocity and attenuation range from 5 to 20 MHz using the published velocity of Ti of 6100 m/s, that would mean the wavelength is on the order of 0.3-1 mm. This scattering zone would be appropriate for the equiaxed β grains, neglecting the effects of athermal ω. Though the β grains are on the same order of magnitude and may only partially fit this categorization.

The geometric region is the most difficult to quantify. In this region, the grain size is large relative to the wavelength and there is a high degree of anisotropy. Long α laths fit in this category if they can be considered as individual grains. However there is no description of what to do in the scenario where β grains fit a different category from a secondary phase in the unified theory [30].

CHAPTER 2. METHODS AND EXPERIMENTAL PROCEDURES

Sample Design and Preparation

A cylindrical shape was selected for the Ti-5553 samples. The ultrasonic transducers used for longitudinal and shear velocity and attenuation measurements are round and produce acoustic waves that propagate from the transducer center so a round sample would minimize asymmetrical geometric reflections. In addition, the SAW velocity measurements are captured with 2 transducers on opposite sides of the sample, so a circle ensures uniformity in SAW velocity measurements as well. The sample thickness of 0.25 in. was thin enough to be able to get acoustic measurements from high attenuation samples and thick enough to get clear resolution between acoustic reflections.

The samples used in this study were made from a single billet of wrought Ti-5553. The aging of this material was unknown so “as-received” samples could be compared to samples that had been subjected to specific heat treatments. The samples were cut using electrical discharge machining (EDM) to ensure high precision sample dimensions. They were removed from the same radial position of a single billet of wrought Ti-5553 as shown in Figure 2.1. The intent of using the same radial position is to achieve the best uniformity in starting microstructure. In addition, uniformity was ensured by selecting pairs of samples selected based on the height within the build. These sample pairs received identical heat treatments.

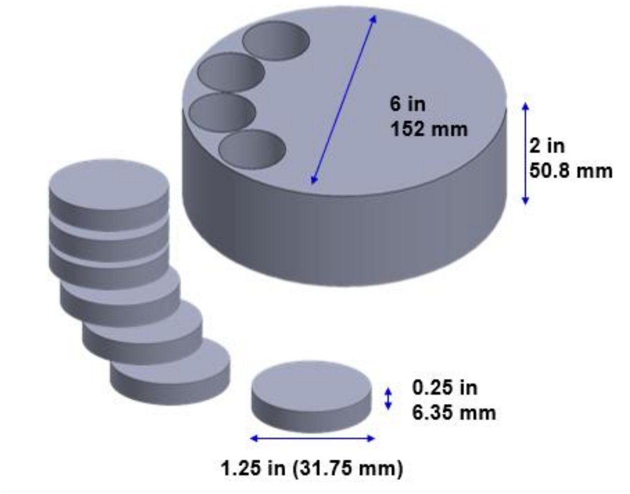

Figure 2.1: Sample dimensions and positioning relative to as-received wrought billet.

Heat Treatments

Samples were ground to 600 grit surface finish with SiC polishing media to remove the residual surfaces from EDM. Heat treatments were conducted by wrapping each of the samples in titanium foil and then encapsulating in a quartz tube along with a piece of titanium sponge. The tube was filled with a slight positive pressure of argon before being sealed (Figure 2.2).

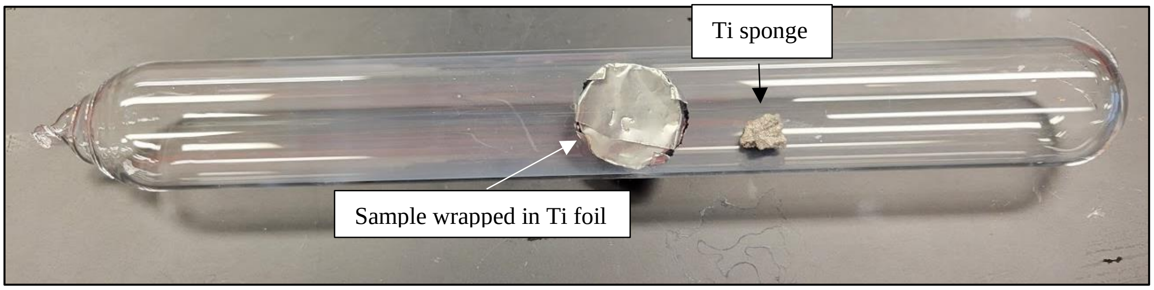

Figure 2.2: Ti-5553 encapsulated in an inert environment prior to heat treatments to prevent oxidization and combustion.

The furnace for this study is a Vulcan 3-1750 box furnace. The samples were all heated above the β transus to 900° C for 30 minutes before being either water quenched or step quenched to a lower temperature by transferring the sample from the 900°C furnace to a Vulcan box furnace preheated to a lower temperature. Water quenching was performed by breaking the encapsulation into a large bowl of water so the sample would make contact with the water immediately after being removed from the furnace. Samples with multiple heat treatments steps were re-encapsulated after water quenching before heating to 550°C or 700°C. The full heat treatment plan is listed in Table 2.1. The samples R1, R2, R3 were tested in the as-received condition.

Table 2.1. Heat treatment plan and expected microstructure

Sample	**Soln Time (h)**	**Soln Temp (°C)**	**Cooling Rate**	**Age 1 Time (h)**	**Age 1 Temp (°C)**	**Cooling Rate**	**Age 2 Time (h)**	**Age 2 Temp (°C)**	**Cooling Rate3**	**Expected Microstructure**
A	0.5	900	WQ	-----	-----	-----	-----	-----	-----	β+athermal ω
B	0.5	900	SQ	4	700	WQ	4	700	WQ	β+coarse α
C	0.5	900	WQ	4	350	WQ	4	700	WQ	β+coarse α (from ω)
D	0.5	900	SQ	8	700	FC: 71.3 ˚C/hr	-----	-----	-----	Bimodal
E	0.5	900	WQ	4	350	WQ	-----	-----	-----	β+isothermal ω
F	0.5	900	SQ	8	550	WQ	-----	-----	-----	β+ fine α
3B,3F	0.5	900	SQ	4	700	WQ	4	550	WQ	Bimodal
3A,3G	0.5	900	WQ	4	350	WQ	4	550	WQ	β+fine α (from ω)
3C, 3E	0.5	900	SQ	8	700	WQ	-----	-----	-----	β+coarse α
R1	-----	-----	-----	-----	-----	-----	-----	-----	-----	-----
R2	-----	-----	-----	-----	-----	-----	-----	-----	-----	-----
R3	-----	-----	-----	-----	-----	-----	-----	-----	-----	-----
4A, 4C	2	900	WQ	-----	-----	-----	-----	-----	-----	β+athermal ω
4E, 4G	8	900	WQ	-----	-----	-----	-----	-----	-----	β+athermal ω

Water quenching created an oxide layer on each sample. This oxide layer is a noticeable gold color for samples quenched from 700° C as can be seen in Figure 2.3.a, and a thicker, multi-colored oxide layer formed on samples quenched from 900°C as can be seen in Figure 2.3.b. The samples were then ground to 800 grit SiC prior to making velocity measurements. Additional grinding to remove scratches and final preparation was conducted for the remaining characterization methods including ultrasonic attenuation.

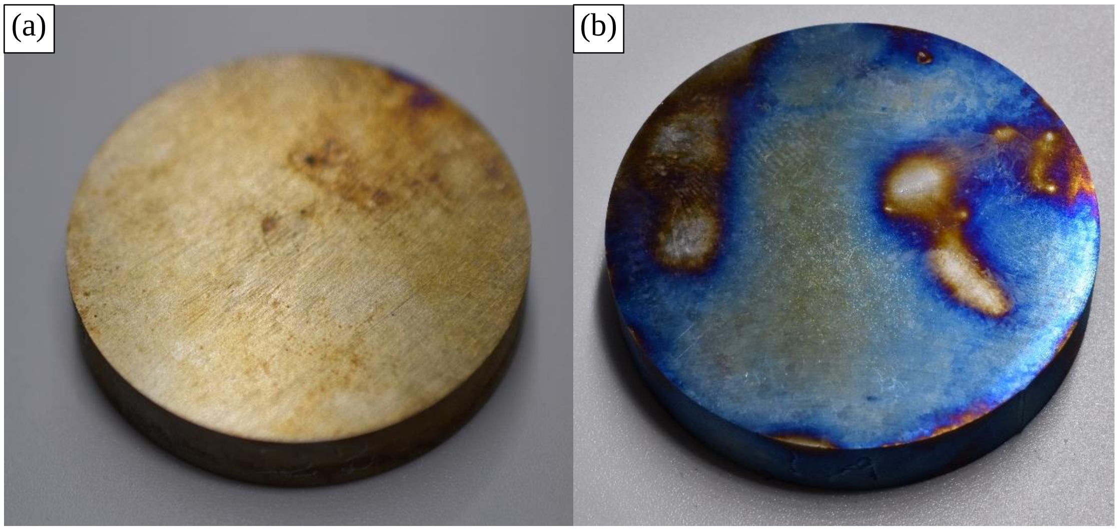

Figure 2.3. Samples after quenching and removing from Ti foil. (a) 1B quenched from 700° C and (b) 1A quenched from 900° C.

Final sample preparation included polishing with 0.04 μm silica, polishing in a vibratory polisher for approximately 1 day, etching with Kroll's Reagent, and then returning to the vibratory polisher until the etched surface is removed. The cleaning process included a minimum of 10 minutes each in water with GP soap solution, acetone, and finally ethanol.

Material Characterization

Samples were imaged with an FEI Inspect 450 SEM with a voltage of 10 kV and spot size of 4.5. SEM images were used to identify the type and quantity of the α phase within the β matrix. A Leica microscope was used to image the β grain size of the samples after they were etched with Kroll’s Reagent. Etching times varied from two seconds to two minutes. The higher the percentage of the α phase, the shorter the etching time was. The fine α samples were particularly challenging to etch with Kroll’s. Etching for 1-2 seconds results in no detectable etching and etching for 2-3 seconds resulted in a sample so burned that it appeared black with casual observation. In order to measure the prior β grains. These samples were etched for 2-3 seconds and then returned to the vibratory polisher until the surface appeared optimally etched.

The β grain size was difficult to ascertain. The β grains were too large to image with SEM and the differences in microstructure meant that most samples required a unique imaging procedure with varying success. Most samples were imaged at 5X magnification with a Zeiss Axiovert 100. The prior β grain boundaries from pure fine α and coarse α samples could not be measured with this microscope, but were observable with a stereomicroscope.

The β grain size was calculated using the prior beta grain boundary factor described by Searles, et al [40], used on Ti-5553 by Kumar [41], and developed by Russ and Dehoff [42] to make a volumetric estimation of the grain size using a 2-dimensional image. This approach is performed manually by overlaying cycloids on an image, counting the grain boundary intersections with the cycloids and then dividing by the total length of the cycloids to get a factor P_L. To get the grain boundary factor S_v, multiply P_L by 2.

The total phase fraction of α and the α lath thickness were calculated using Mipar image analysis software. This software is able to segregate the α phase from the β phase and then calculate the percentage of the image is α for the phase fraction of α calculation. For the α lath thickness measurement, Mipar can use randomly rotating lines to count the intersections between these lines with the α and β phase boundaries to calculate the mean inverse intercept ($\frac{1}{\lambda}mean$). The α lath thickness is then calculated using Equation 9 [40,42]:

$$thickness = \frac{1}{(1.5*\frac{1}{\lambda}mean)} \qquad \text{Eq. 9}$$

Ultrasonic Velocity

Ultrasonic velocity measurements are simply a ratio of distance over a corresponding change in time. Velocity is an inherent material property, but it is wave mode dependent. In this study, velocities were captured using the longitudinal, shear and Rayleigh wave modes. Due to the diverse range of material properties and the three wave modes, a variety of strategies were used to measure the change in time required to calculate velocity. Change in distance is obtained merely by measuring the thickness or diameter of each sample as an average of 5 readings measured with a micrometer. All time measurements were made using the contact method. Longitudinal measurements were made using a 5 MHz, 0.5 inch diameter, unfocused transducer and shear measurements were made using a 5 MHz, 0.25 inch diameter, unfocused, shear transducer. Rayleigh measurements used 1 MHz or 2.25 MHz longitudinal transducers coupled to the corners of each sample using the configuration in Figure 2.4 and ultragel II couplant.

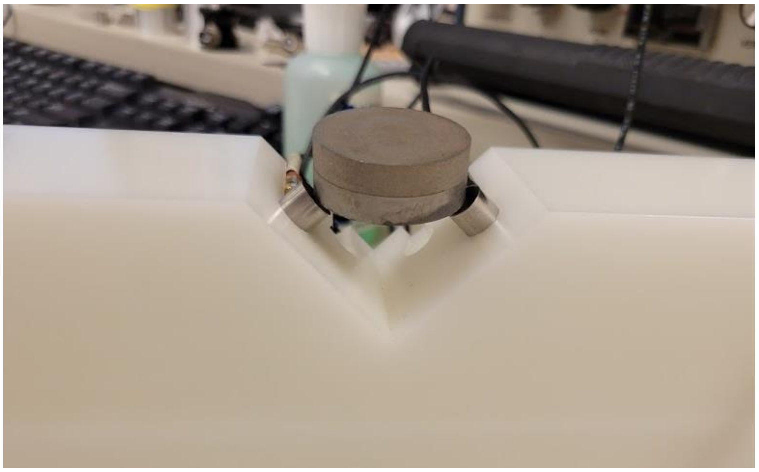

Figure 2.4. SAW Velocity measurement fixture.

Three methods were used to measure the change in time used for the velocity calculations. Method 1 was used for all longitudinal velocities and most of the shear velocities. A single pulse echo transducer was used to transmit and receive ultrasonic waves from a single side of each sample. In method 1, a waveform with a minimum of two backwall (BW) reflections was captured to calculate the change in time required for a measurement of velocity. An example waveform and comparison of signals for the time measurement can be seen in Figures 2.5 and 2.6. Since Method 1 is pulse echo, the sound wave passes through the sample twice and recorded change in time needs to be divided by 2.

Measurement Method 2 was used for samples 1A, 2A, 1E and 2E to measure shear wave velocity because these samples did not have two strong BW reflections when measured with a shear wave transducer. In other words, these samples had high attenuation. For this reason, a version of the through transmission measurement technique was used. Through transmission ultrasound uses two transducers placed on opposite sides of the sample. One transducer transmits an ultrasonic wave and the other receives it. A piece of fused quartz was joined to the sample with couplant, and the transmitting transducer was placed on the quartz and the receiving transducer was placed on the sample (Figure 2.7). A signal could be detected from the wave exiting the quartz and entering the sample, and a second signal could be detected when the wave exited the sample. The quartz was then measured in the through transmission configuration without the sample. The waveform with fused quartz could be subtracted from the signal with fused quartz and the sample to measure the change in time corresponding to the sample.

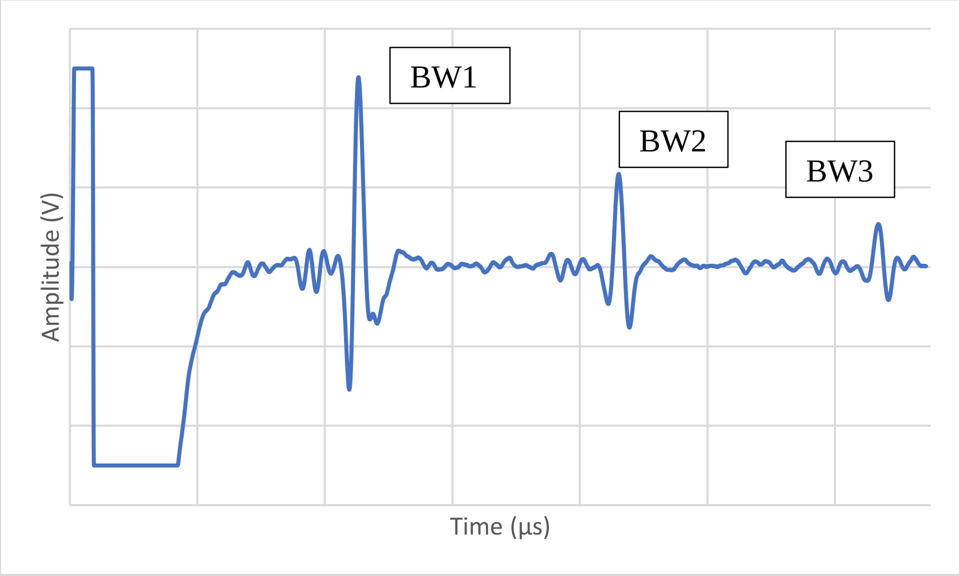

Figure 2.5: Example ultrasonic waveform with three BW reflections. This waveform comes from sample 2F with a longitudinal wave using Method 1.

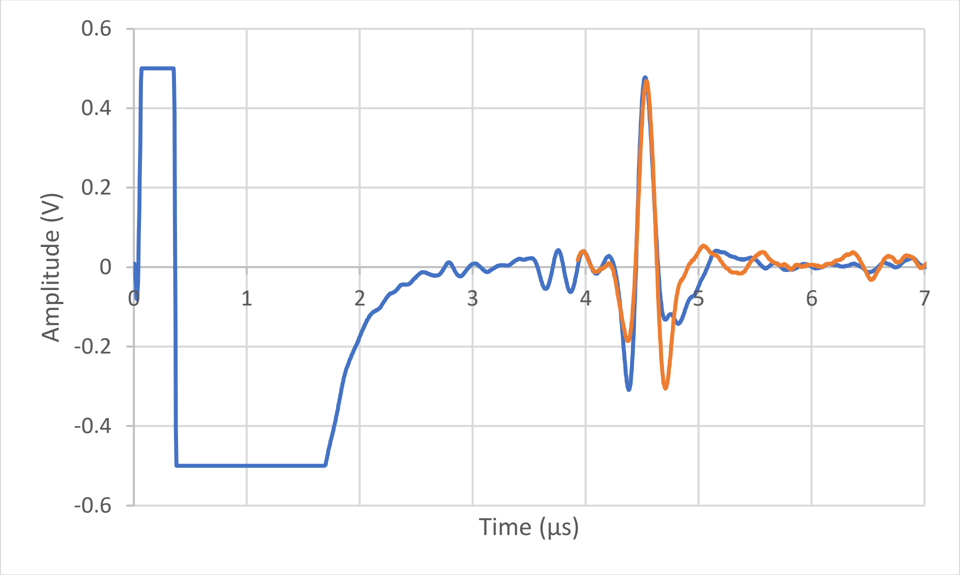

Figure 2.6: BW2 scaled and overlaid on BW1 for sample 2F. The shift along the time axis was recorded as the change in time.

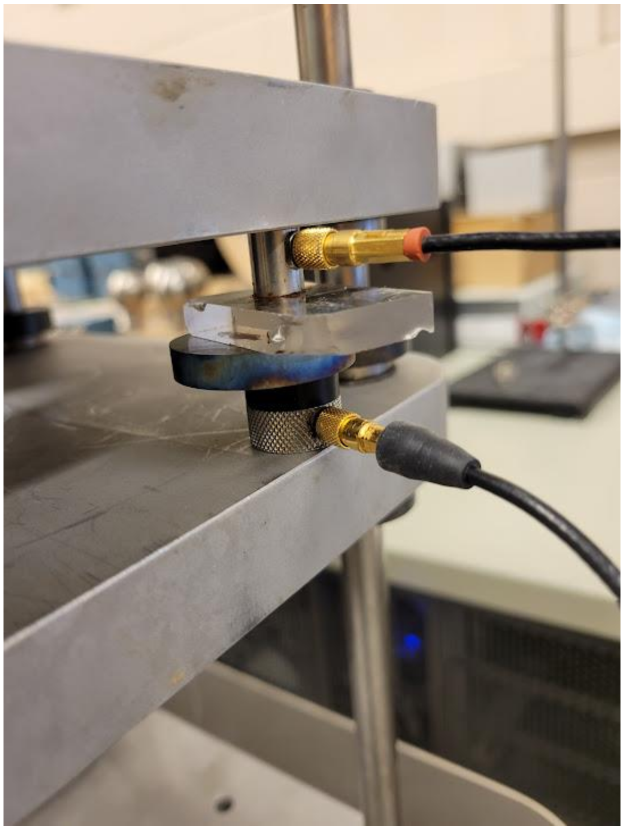

Figure 2.7. Sample coupled to fused quartz and shear transducers with reference for Method 2 time measurement.

Rayleigh velocity was measured using Method 3. Rayleigh waves (a type of surface acoustic wave or SAW) travel across the surface of a sample as the name implies. These waves attenuate quickly and have a greater distance to travel across the diameter of the sample so lower frequency (2.25 MHz and 1 MHz) contact transducers were used to generate this wave mode. These transducers are designed to generate longitudinal waves, but they were positioned to introduce ultrasonic waves at a 45° to the surface to generate a SAW. The receiving transducer is also in contact with the sample at a 45° angle to the surface so it will only detect the SAW wave mode. Multiple wave modes will be generated with this technique which may create some doubt about whether it is in fact a SAW that is being detected by the receiving transducer. This can easily be verified by wetting a finger with water or couplant and touching the surface of the sample. If the signal decays or disappears, it is safe to assume that this signal is from a surface wave which has been dampened. Like Method 2, a reference sample with a different length was measured to provide a signal at a reference distance. The reference was made using an EDM disc cut to a width of 11.76 mm as can be seen in Figure 2.8.

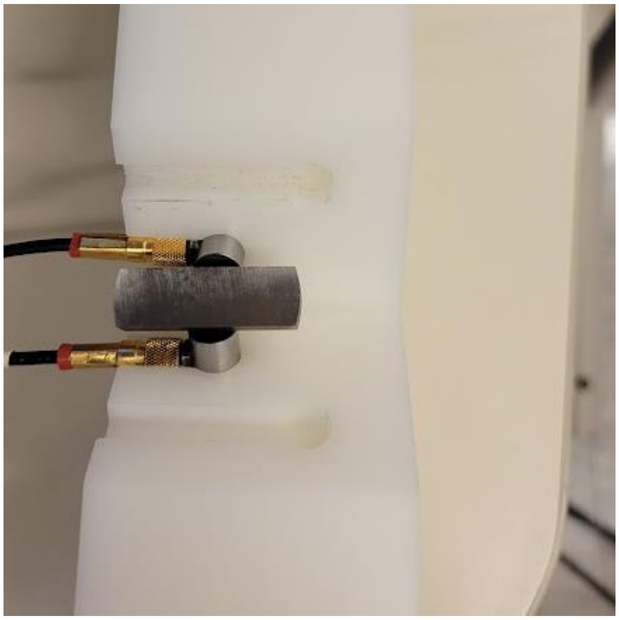

Figure 2.8. Measurement of reference sample for SAW velocity calculation.

The 3 measurement methods described could be performed with any ultrasonic pulser/receiver. Based on availability of equipment, the longitudinal and shear waveforms were measured with a Panametrics model 5800 pulser/receiver and the SAW waveforms were measured with a UTEX UT340.

Ultrasonic Attenuation

Ultrasonic attenuation was measured using an immersion ultrasonic test setup and a minimum of one broadband ultrasonic transducer. Since the samples are round and match the shape of the propagating sound wave, ultrasound will move from the center of the sample and interact with the edges of the sample uniformly. This makes the number of backwall reflections before encountering edge effects relatively easy to calculate using Snell's law. A minimum of two frontwall (FW) and two BW reflections were captured to make an attenuation calculation. In addition to these waveforms, this measurement also required the following inputs:

- Material density and thickness
- Water temperature (for density)
- Distance between the transducer and the sample in water (i.e. water path)
- Signal gain (in dB) when the waveform was captured
- Transducer diameter

To set up the test, the sample was positioned within the immersion tank to be perpendicular to the transducer generating the sound wave. In addition, the support of the sample in the tank was critical to consider since laying the sample directly on the surface of a similar material creates the potential for the sound wave to exit the back of the sample and enter the supporting fixture, interfering with the measured waveform. To mitigate this problem, the sample can either be supported so that there are a few inches of water directly under the center of the sample, or an air bubble could be trapped under the sample since the impedance and velocity difference between titanium and air is great enough that most of the sound wave will be disinclined from exiting the bottom of the sample into air. The former technique was used for this study and a picture of this test setup can be seen in Figure 2.9. The instrument used to capture the attenuation data is a UTEX UT340 Pulser Receiver System.

Transducer selection was another important piece of the inspection. An optimal transducer for attenuation measurements will be broadband and unfocused. The general preference for any ultrasonic test is to select a transducer with the highest frequency (which corresponds to the shortest wavelength) that can adequately penetrate a material and be compatible with the available pulser/receiver. A transducer used for attenuation measurements has the minimum frequency requirement of being able to resolve two BW reflections. A single transducer was not adequate for measuring the attenuation of these Ti-5553 samples because of the significant attenuation difference between the β phase samples and the samples containing the α secondary phase. The β samples were measured with 5 MHz and 2.25 MHz to achieve both adequate ultrasound penetration and a broad-enough spectrum of frequencies to create an attenuation curve. The α samples attenuated much less than the samples with no α so a 20 MHz transducer was used. As frequency increases, the ultrasonic wave attenuates more quickly so increasing the frequency of the transducer for the low attenuation samples, resulted in enough attenuation to be measurable.

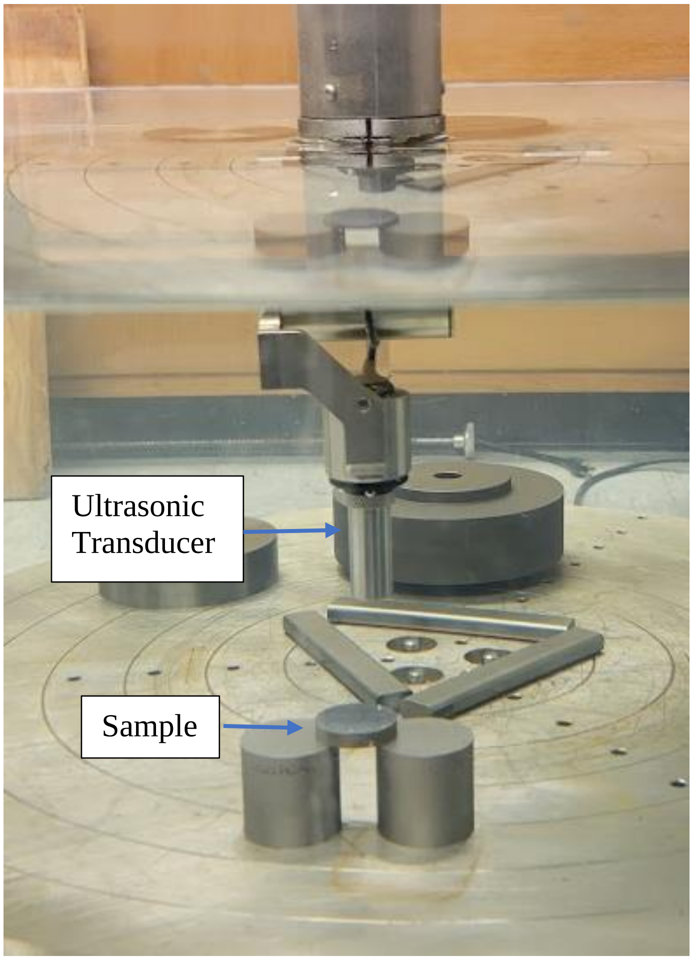

Figure 2.9: Attenuation Measurement Configuration in an Ultrasonic Immersion Tank Filled with Water

Once all of the data was collected, the waveforms were used to measure an accurate water and material velocity. These velocities and densities were used to calculate the acoustic impedance of the sample and water and the acoustic impedances were used to measure the reflection and transmission coefficients (R_{SW}, T_{SW}, T_{WS}) at the water and sample interface. Next an FFT was taken of the first FW and the two BW signals. The magnitude of the FFT terms was then corrected for beam diffraction using the Lommel Diffraction technique [43]. Finally all the calculated terms can be used in the attenuation equations 10-12 for the FW and 2 BW reflections. Here α_w is the attenuation in water, x is the distance traveled in water or the sample, D is the diffraction coefficient, A is signal amplitude, A_0 is an unknown value that eventually cancels out of the equation, and α_s is the sample attenuation that ultimately must be calculated.

The calculation of α_s was done using a technique that has been performed and taught at the Center for Nondestructive Evaluation and is mentioned in publications by Margetan, Panetta, and Thompson [44,45]. In order to solve for the sample attenuation α_s, divide the equation for FW1 by the equation for BW1, FW1 by BW2, and BW1 by BW2. This approach cancels out the A_0 term and allows for solving α_s as a ratio of 2 waveforms.

$$A_{FW1} = A_0 e^{-2\alpha_w x_w} R_{WS} D_{FW1} \qquad \text{Eq. 10}$$

$$A_{BW1} = A_0 e^{-2\alpha_w x_w} T_{WS} R_{WS} T_{SW} e^{-2\alpha_s x_s} D_{BW1} \qquad \text{Eq. 11}$$

$$A_{BW2} = A_0 e^{-2\alpha_w x_w} T_{WS} R_{SW}^3 T_{SW} e^{-4\alpha_s x_s} D_{BW2} \qquad \text{Eq. 12}$$

Once all three of the attenuations were calculated, they were plotted together as can be seen in Figure 2.10. Notice that over some region (approximately 7 to 15 MHz in this example), the three curves overlap or average to a curve that could be fit to a power law form which can be used to describe attenuation as a function of frequency (Figure 2.11). Attenuation is given by the units Nepers/cm. This entire region may not be valid for calculating the power-law fit since the frequency content of BW1 will always be less than FW1 and BW2 less than BW1. The frequency range used to calculate the attenuation power law fit was optimized using the diffraction-corrected FFT curves so only valid frequencies were used in generating the power law curve fit. In the high attenuation cases, a 5 MHz broadband transducer was not able to generate enough frequency content to generate this plot, so a second measurement with a 2.25 MHz transducer was used to expand the range of frequencies over which attenuation could be measured. A similar approach was used with the low attenuation samples, but ultimately the data from a single 20 MHz transducer was used for the attenuation measurements in this document.

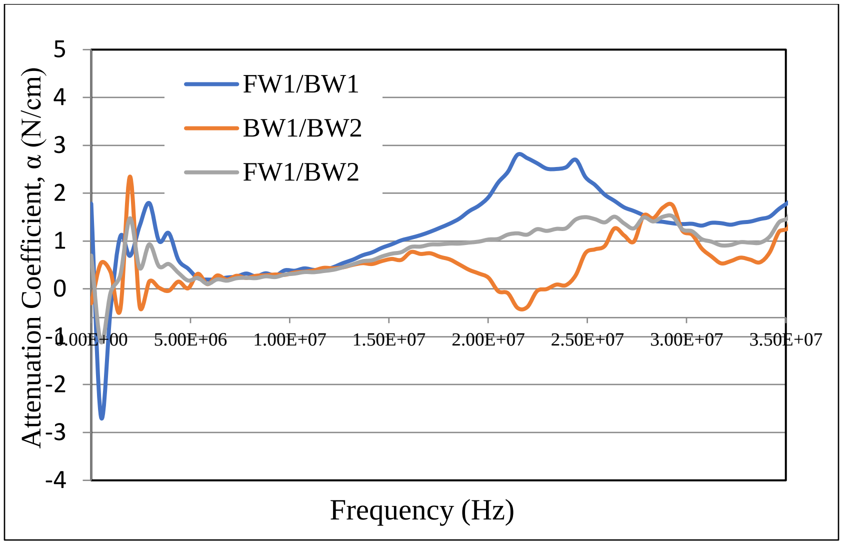

Figure 2.10. Attenuations curves from coarse α sample 3E.

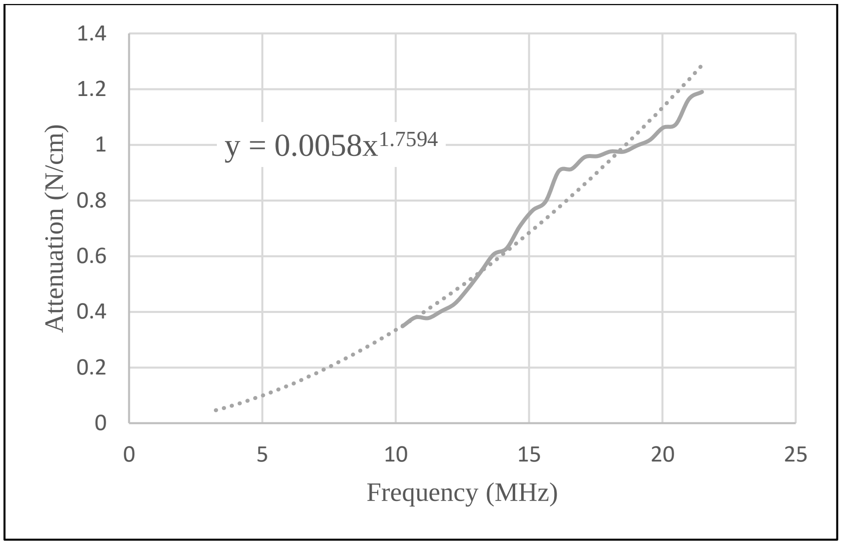

Figure 2.11. Average of curves from Figure 2.10 over valid region and fitted to power law curve.

SRAS

Spatially resolved acoustic spectroscopy (SRAS) is a laser ultrasound technique that generates surface waves including but not limited to Rayleigh waves and uses them to measure velocities of individual grains or crystallites inside of large grains. In this technique, velocity is measured in the frequency domain instead of the time domain. SRAS measures SAW waves with an optimized wavelength (λ) matching the spacing of a grating source[27,46]. Velocity is then measured by monitoring the SAW signals for the dominant received frequency (*f*) at each point in a scan. Velocity is then given by v=λ*f*. These measured velocities will change abruptly between grains with differing crystallographic orientation allowing for a measurement of crystallographic orientation and texture with less surface preparation and faster coverage of larger areas than the standard electron backscatter detection technique used for measurement of texture [27,46]. The data used in this report was collected by the University of Nottingham.

Hardness and Cyclic Indentation

Hardness testing was conducted using a Zwick Roell indenter capable of creating a traverse of hardness and cyclic indentation. An array of 25 Vickers hardness indents were made with a loading of 0.3 kN and a dwell time of 15s. The following sample types were tested for hardness: β phase, coarse α, fine α, fine α from ω, and an as-received sample.

The same machine was used with a ball indentation attachment to perform cyclic indentation testing [47]. An increasing load is applied with successive indents, creating a curve that can be used to identify the 0.02% offset yield point of the sample. This test is repeated in a planned array allowing for the measurement of yield stress at several locations across the sample surface. Each sample was measured 20 times. The starting load was 25N increasing at an interval of 50N to 375N. The accumulated indentation curves (Figure 2.12), the elastic modulus and Poisson’s ratio of the indenter, and the Young’s modulus and Poisson’s ratio calculated using the measured longitudinal and shear velocities were used to plot an indentation curve such as Figure 2.13.

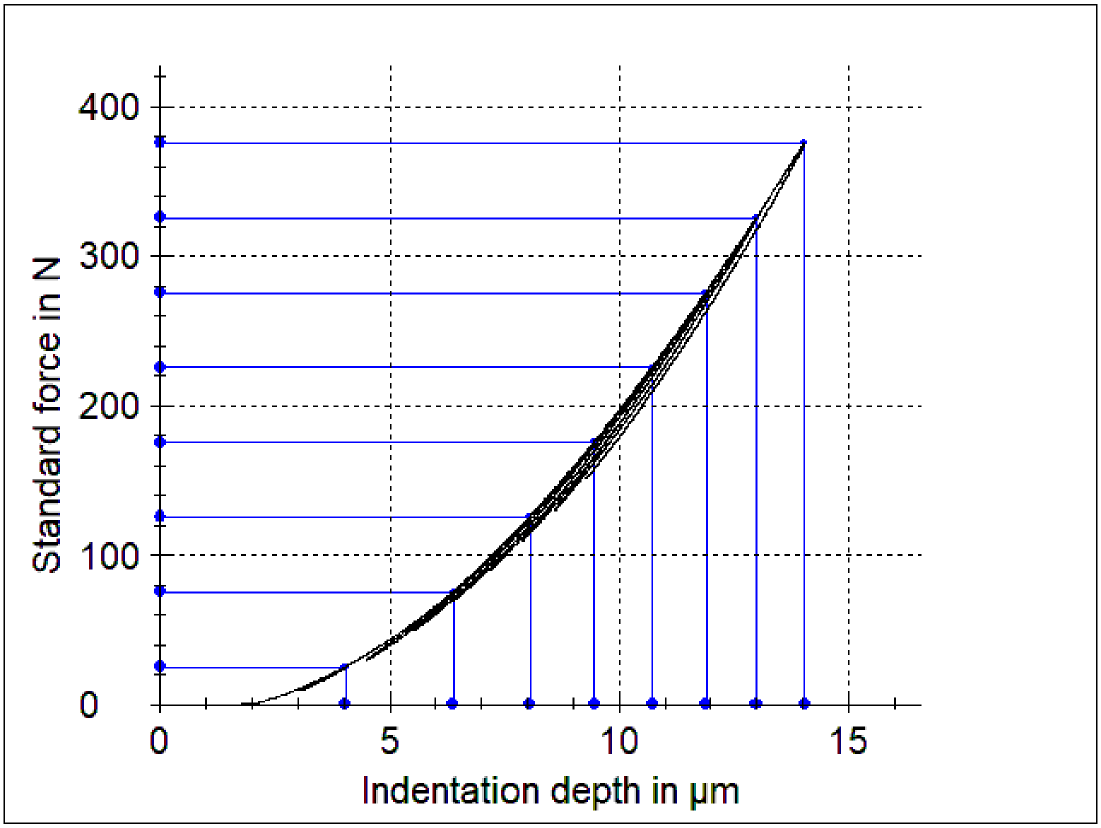

Figure 2.12: Cyclic curves with increasing loading on sample 1F.

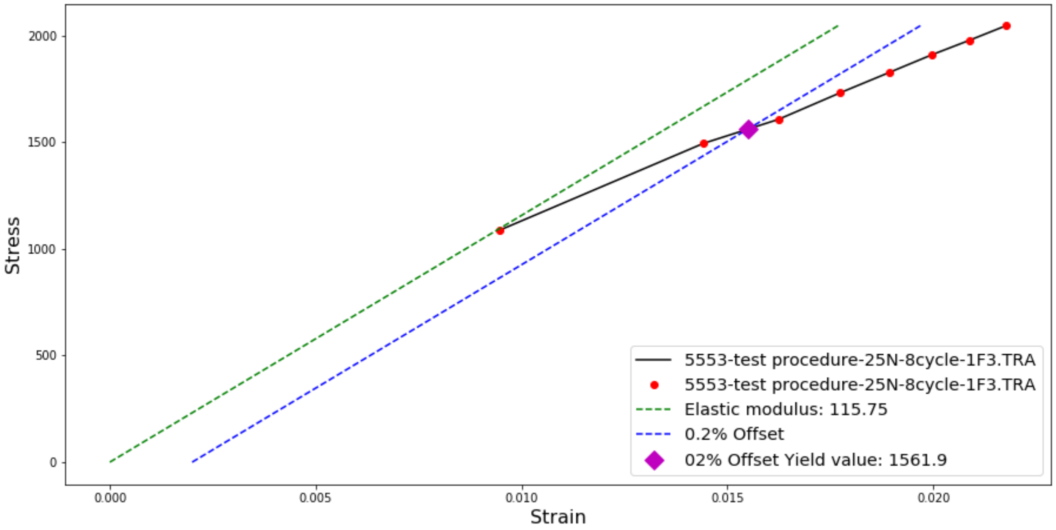

Figure 2.13: Cyclic curve with plotted 0.02% yield point identified using E and ν calculated from ultrasonic velocities.

In addition, Berkovich nanoindentation was performed by Niraj Pramod Atale from Dr. Sid Pathak’s research group to measure the hardness and modulus in order to compare to the modulus and hardness calculation and measurement described previously. At an indentation depth of 500 nm, both α and β phases were measured, but shallower indentation depths would allow for measuring the hardness and modulus of the α and β phases individually in a coarse α sample.

CHAPTER 3. RESULTS AND DISCUSSION

Microstructure

The heat treatment plan was designed to precipitate microstructures that are categorized in this report as fine α, coarse α, β, and bimodal. The samples with only β and athermal or isothermal ω were not imaged with SEM since the only feature to measure are the β grain boundaries which are large relative to the SEM field of view. Figure 3.1 shows the Backscattered electron (BSE) SEM images of the coarse α samples. It was observed that the samples subjected to a step quench (SQ) from 900° C to 700° C resulted in long coarse alpha laths precipitating from the β grain boundaries. The samples with a HT step at 350° C between 900° C and 700° C intended to precipitate isothermal ω, displayed short, coarse α laths that appear to have formed uniformly from within the interior of the grains. These images were taken at magnification of 5000X.

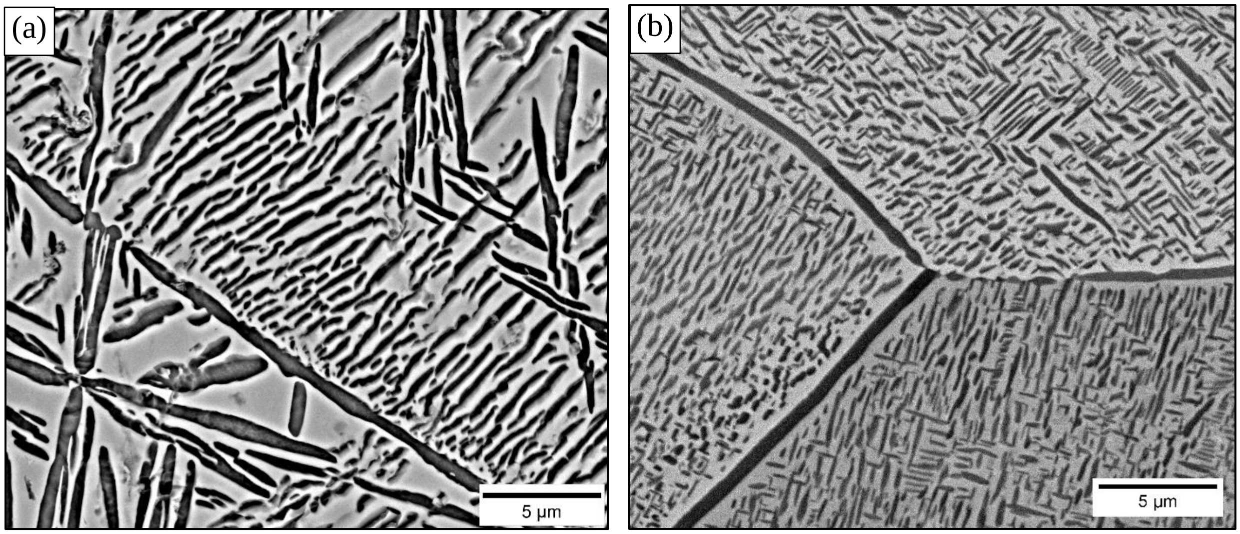

Figure 3.1. Backscattered electron (BSE) SEM micrographs of (a) 3C with coarse alpha laths precipitating from β grain boundaries and (b) 1C with coarse alpha laths precipitating from prior isothermal omega sites. The bright phase is the β phase and the dark phase is the α phase.

Figure 3.2 shows the BSE SEM images for the fine α samples. Like the coarse α samples, there were samples that were step quenched from 900° C to the fine α-precipitating temperature of 550° C temperature and samples were subjected to a temperature of 350° C to form isothermal ω between 900° C and 550° C. In this case, the fine α samples are represented at multiple magnifications. In Figure 3.2.a, the fine α phase without isothermal ω, 1F, is shown at 5000X. In Figure 3.2.b, the same sample is imaged at 10,000X. Figure 3.2.c, is an image of the isothermal ω, then fine α sample 3A. This fine α is at a significantly smaller scale than 1F, so sample 3A (and the partner sample 3G) were imaged at the highest reasonable magnification for this instrument 30,000X. This magnification was not high enough to adequately image 3A and 3G so data could not be calculated for these microstructures.

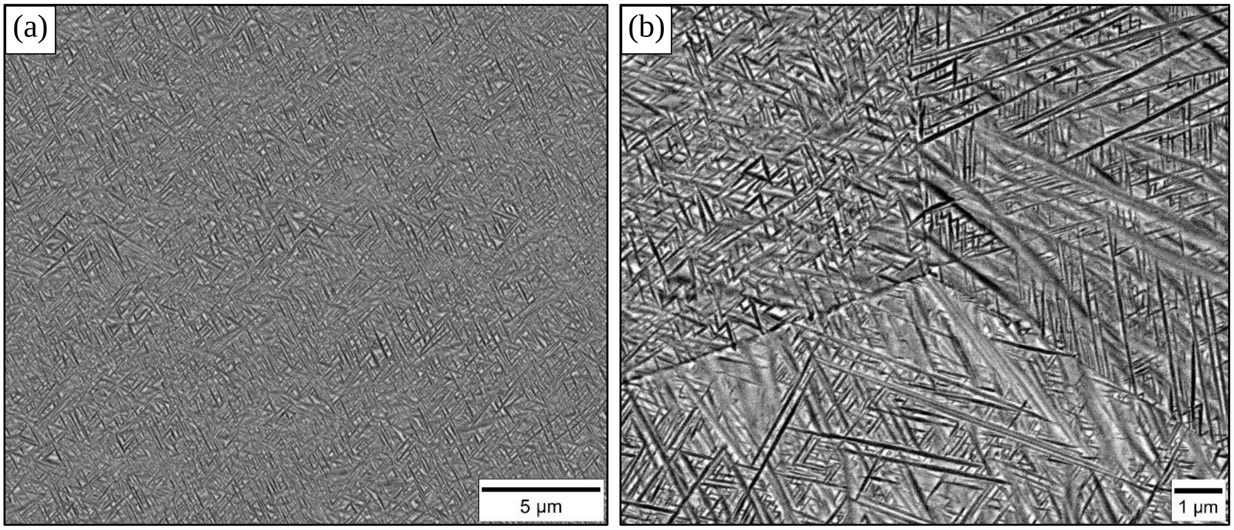

Figure 3.2. BSE SEM images of fine α samples (a) 1F at 5000X magnification, (b) 1F at 10000X, (c) 3A at 10000X, and (d) 3A at 30000X. The fine α precipitating from prior β grain boundaries in 1F and prior isothermal ω sites in 3A.

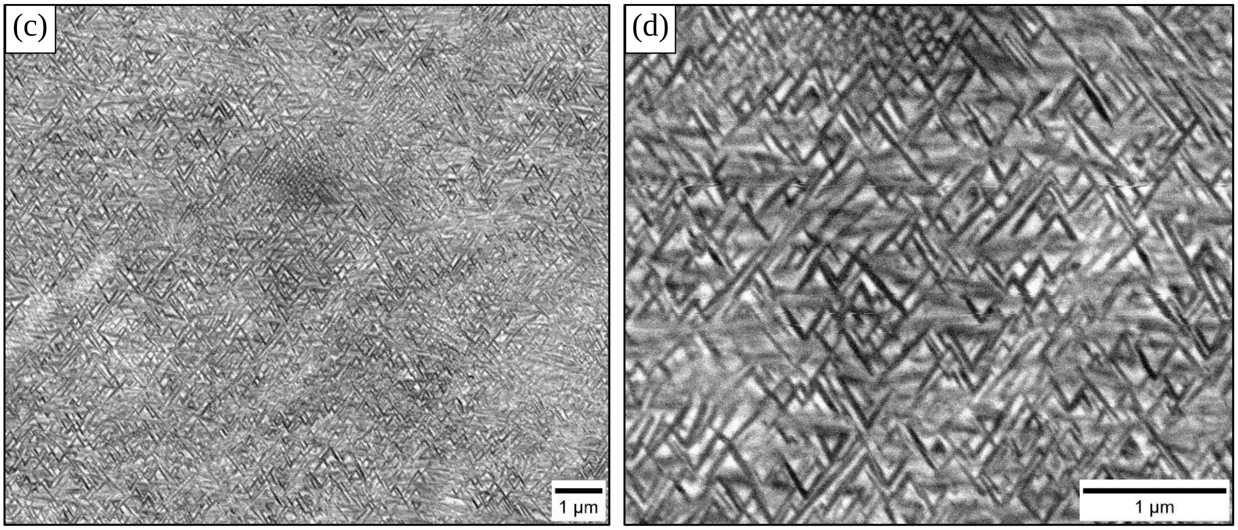

Figure 3.3. Continued.

Figure 3.3 contains BSE SEM images of the samples with bimodal microstructures. Figure 3.3.a was precipitated with a furnace cool starting at the coarse α temperature of 700° C to room temperature at a rate of 71.3° C/hr. This microstructure contains a relatively uniform dispersion of coarse and fine α laths. The bimodal microstructure from samples 3F and 3B closely resemble the coarse α microstructure from 1B, 2B, 3C and 3E with pockets of fine α precipitation from within some of the regions of retained β phase.

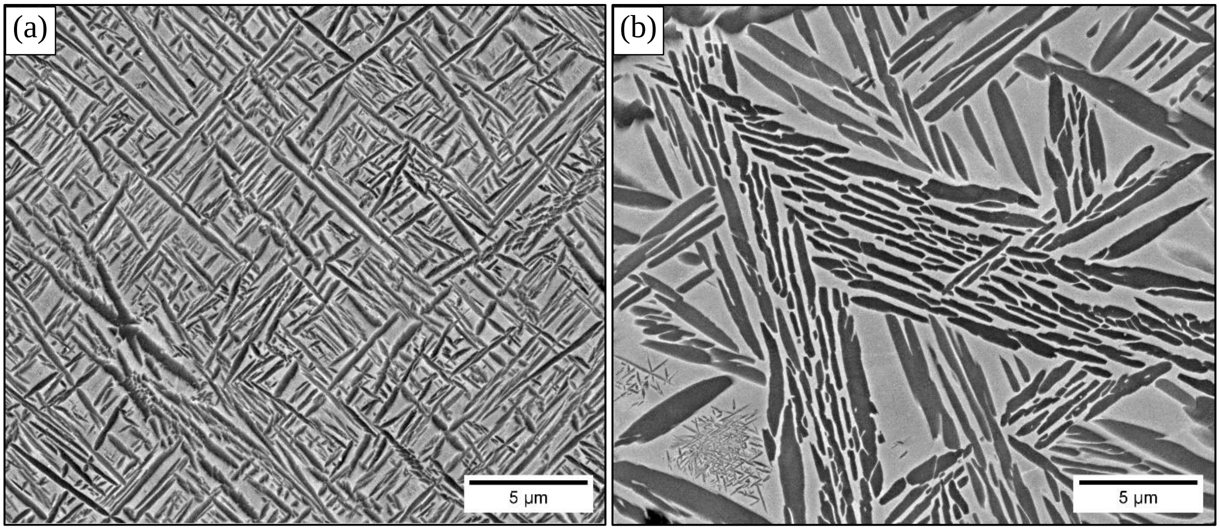

Figure 3.4. BSE SEM images of bimodal microstructures (a) 2D furnace cooled from 700°C to room temperature for 8 hours and (b) 3F which was heated at 700°C for 4 hours and 550° C for 4 hours.

In Figure 3.4, the BSE SEM images representing the as-received samples can be observed at a magnification of 5000X. There is no noticeable difference between these samples. The as-received microstructure appears to be most similar to the bimodal microstructure from the furnace-cooled samples 1D and 2D.

The BSE SEM images for each sample were used to calculate the phase fraction α and the mean free path. Optical images were used to measure the β grain size using the cycloid technique. These results can be found in Table 3.1.

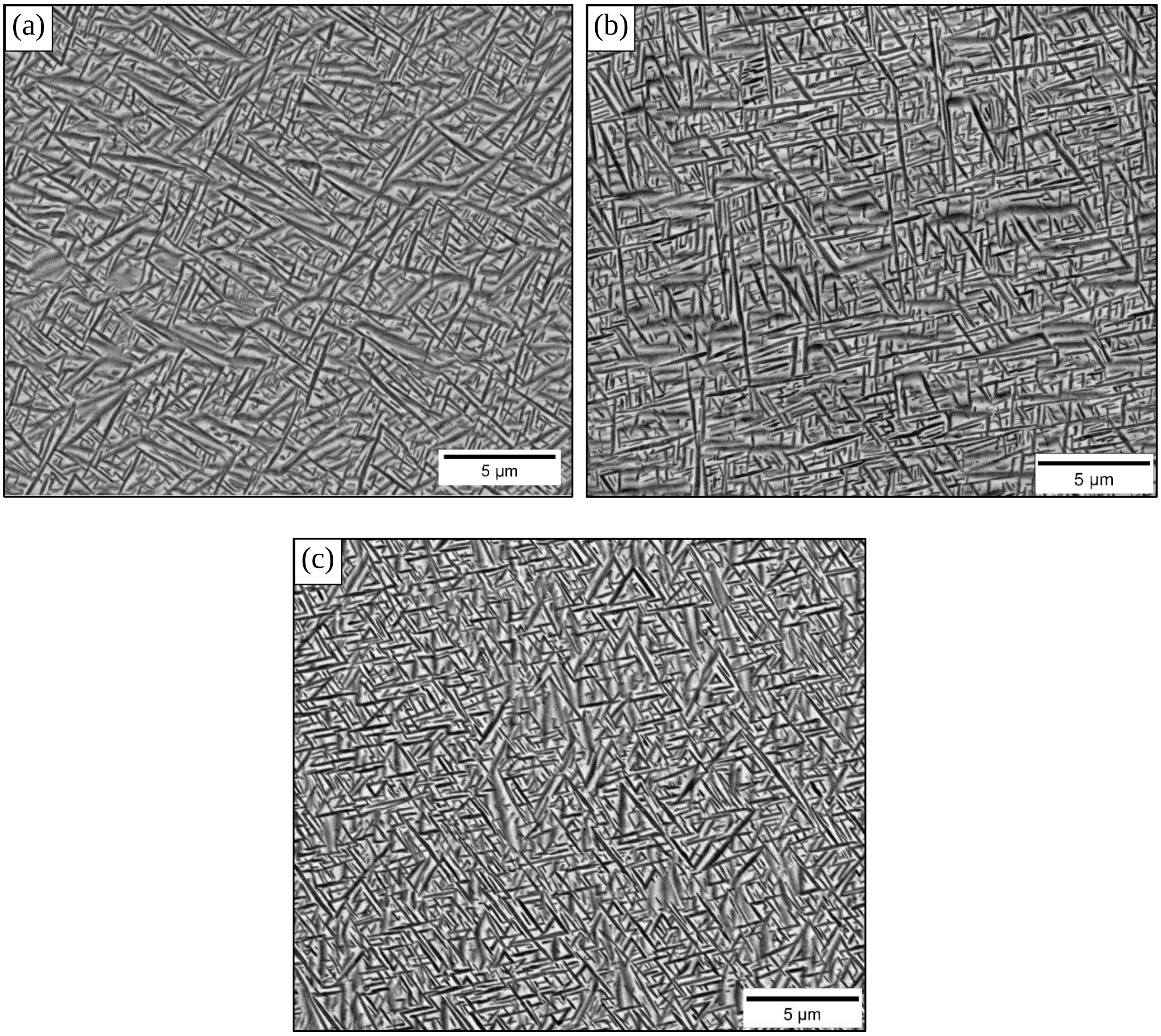

Figure 3.5. BSE SEM images of as-received samples (a) R1, (b) R2, (c) R3

The β grains were too large to measure with SEM, and were measured with difficulty using optical imaging. The samples with no α phase could be imaged relatively easily, but the prior β grain sizes were obscured by the α phase. These grain boundaries were not completely obliterated and could be definitively observed at low frequency with a stereomicroscope or SEM imaging (see Figure 3.2.b), but optical microscopes tended to be overwhelmed by the contrast in the α phase making clear discernment between prior β grain boundaries. It should be noted that the samples with coarse α precipitating from isothermal ω, were the easiest samples containing α to image and the samples precipitating purely coarse α without a prior or subsequent heat treatment step were among the most difficult to image, supporting the assertion that isothermal ω caused the α phase to preferential precipitate uniformly within the β instead of the typical precipitation from the prior β grain boundaries. Example optical images used for calculating β grain factor can be seen in Figure 3.5.

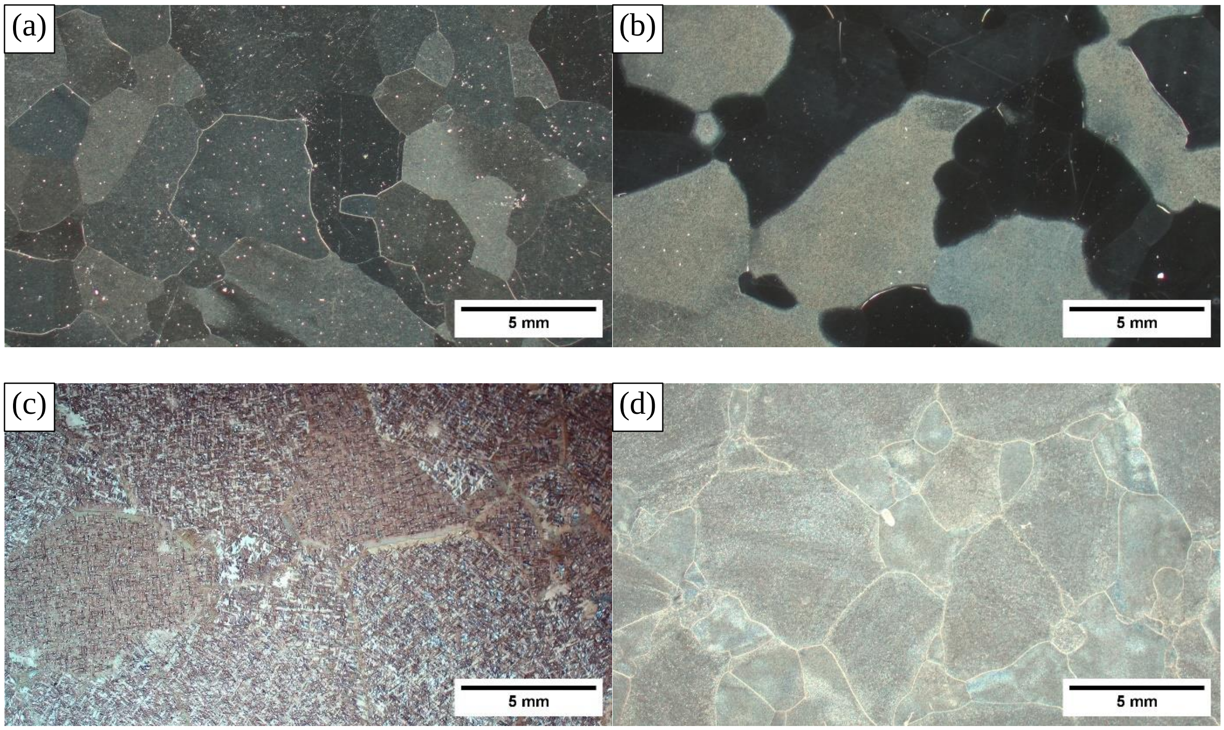

Figure 3.6. Example optical images taken with a Leica at 5X magnification of (a) β sample 2A, (b) β and isothermal ω sample 2E, (c) coarse α sample 2B, and (d) coarse α from isothermal ω sample 1C.

The calculated grain factor is a representation of the 3D β grain size where a sample with a lower factor would have a larger grain size than a sample with a higher factor. Samples 4A and 4C were heated at 900° C for 2 hours before water quenching with the goal of doubling the grain size from samples 1A and 2A and samples 4E and 4G were heated for 8 hours to double the size of 4A and 4C.

Table 3.1. Cumulative microstructural results

Sample ID (X2)	Heat Treatment	Expected Microstructure	Phase Fraction α	PF St. Dev	α-lath Thickness µm	Avg β Grain Factor (mm2/mm3)	β Grain Size St. Dev
A	900-0.5WQ	β+ath ω	NA	NA	NA	0.61,0.59	0.08,0.06
B	900SQ,700-4WQ, 700-4WQ	β+coarse α	38.5, 39.6	0.61, 0.28	0.20, 0.21	0.47, 0.52	0.06. 0.15
C	900WQ, 350-4WQ, 700-4WQ	β+coarse α	41.7, 35.5	1.48, 0.31	0.04, 0.05	0.64,0.62	0.10,0.15
D	900SQ, 700-8FC	β+coarse α + fine α	48.1, 50.7	3.92, 2.82	0.06, 0.08	0.56, 0.73	0.12, 0.04
E	900WQ, 350-4WQ	β+iso ω	NA	NA	NA	0.52,0.57	0.04, 0.06
F	900SQ,550-8WQ	β+fine α	57.8, 60.5	0.6, 0.66	0.01, 0.02	0.49, 0.52	0.02, 0.01
3B,3F	900SQ, 700-4WQ,550-4WQ	β+coarse α+fine α	51.7, 46.7	1.21, 1.3	0.21, 0.19	0.66, 0.47	0.11, 0.04
3A,3G	900SQ, 350-4WQ,550-4WQ	β+fine α	-	-	-	0.54, 0.47	0.03, 0.10
3C, 3E	900SQ, 700-8WQ	β+coarse α	38.7, 37.7	0.46, 0.6	0.20, 0.17	0.51, 0.50	0.10, 0.01
R1	NA	Bimodal	53.8	1.05	0.08	0.5	0.11
R2	NA	Bimodal	52.4	0.76	0.06	0.39	0.03
R3	NA	Bimodal	53.2	0.75	0.07	0.41	0.05
4A, 4C	900-2WQ	β+ath ω				0.41,0.28	0.05, 0.03
4E, 4G	900-8WQ	β+ath ω				0.22,0.24	0.04, 0.12

Ultrasonic Velocity

Velocities were calculated for longitudinal, shear and Rayleigh waves. In addition, velocity maps using the dominant surface wave modes were captured using SRAS. Beginning with the longitudinal and shear velocities, it can be observed that significant changes in velocity were measured. The min and max long velocities were 5726 and 6111 m/s, and the min and max shear velocities were 2733 and 3088 m/s, corresponding to a 6.5% difference for longitudinal waves and 12.2% for shear waves. Using these velocities and densities to calculate Young’s modulus, shear modulus and poisson’s ratio. These two velocities show a differentiation between the β microstructures and samples with α phase. Once the α phase is introduced, the velocity of the samples appears to increase. This may be attributable to the HCP α phase having a denser atomic packing factor than the BCC β phase. There is also an increase in velocity for the samples with hexagonal ω phase.

Table 3.2. Longitudinal and shear velocities according to heat treatment

Sample ID (X2)	**Heat Treatment**	**V-L1 (m/s)**	**V-L2 (m/s)**	**V-sh1 (m/s)**	**V-sh2 (m/s)**	**Expected Microstructure**
A	900WQ	5793.0	5726.0	2732.8	2744.5	β+athermal ω
B	900SQ,700-4WQ, 700-4WQ	5971.9	5966.8	2819.0	2927.9	β+coarse α
C	900WQ, 350-4WQ, 700-4WQ	5961.3	5974.5	2877.9	2924.6	β+coarse α
D	900SQ, 700-8FC	6101.0	6066.0	3050.5	3069.9	β+coarse α + fine α
E	900WQ, 350-4WQ	5853.4	5931.7	2860.2	2924.5	β+isothermal ω
F	900SQ,550-8WQ	6111.1	6094.8	3055.6	3084.8	β+fine α
3B,3F	900SQ, 700-4WQ,550-4WQ	6057.5	6053.3	3021.5	3019.4	β+coarse α+fine α
3A,3G	900SQ, 350-4WQ,550-4WQ	6081.0	6097.1	3070.3	3056.0	β+fine α
3C, 3E	900SQ, 700-8WQ	5971.6	6001.7	2916.7	2931.1	β+coarse α
R1	NA	6041.7		3088.0		NA
R2	NA	6065.9		3077.5		NA
R3	NA	6110.6		3062.8		NA
4A, 4C	900-2WQ	5522.2	5515.3	2710.9	2732.0	β+athermal ω
4E, 4G	900-8WQ	5738.0	5562.4	2833.6	2656.8	β+athermal ω

Table 3.3. Elastic constants calculated from longitudinal (L) and shear (sh) velocities in 3.2

Sample ID (X2)	Heat Treatment	E-L1 (GPa)	E-L2 (GPa)	G-sh1 (GPa)	G-sh2 (GPa)	υ-1	υ-2
A	900WQ	94.06	94.34	34.66	34.92	0.36	0.35
B	900SQ,700-4WQ, 700-4WQ	100.16	106.79	36.91	39.80	0.36	0.34
C	900WQ, 350-4WQ, 700-4WQ	103.68	106.65	38.45	39.72	0.35	0.34
D	900SQ, 700-8FC	115.31	116.35	43.24	43.81	0.33	0.33
E	900WQ, 350-4WQ	101.98	106.35	37.96	39.70	0.34	0.34
F	900SQ,550-8WQ	115.75	117.47	43.41	44.24	0.33	0.33
3B,3F	900SQ, 700-4WQ,550-4WQ	113.06	113.01	42.37	42.35	0.33	0.33
3A,3G	900SQ, 350-4WQ,550-4WQ	116.41	115.71	43.80	43.43	0.33	0.33
3C, 3E	900SQ, 700-8WQ	106.10	107.12	39.49	39.87	0.34	0.34
R1	NA	117.43		44.37		0.32	
R2	NA	116.80		44.02		0.33	
R3	NA	115.96		43.52		0.33	
4A, 4C	900-2WQ	91.47	92.64	34.10	34.63	0.34	0.34
4E, 4G	900-8WQ	99.75	88.58	37.26	32.75	0.34	0.35

Velocity measurements were compared to the β grain sizes, α lath thickness and α phase fraction since these are the metallurgical features that are likely to have the greatest impact on performance. Since velocity is related to modulus and attenuation is related to grain scattering, the expectation is that velocity would have little dependence on β grain size but correlates to the α measurements. In Figure 3.6, there is a clustering based on α type, particularly for longitudinal velocity, but this trend appears to have more to do with differences in the α phase than actual β grain size. Figure 3.7 shows that when comparing velocity to α lath thickness or phase fraction, traditional velocity measurements do positively correlate.

The Rayleigh or experimental SAW velocities were also measured for each sample for the purpose of comparing to the SRAS results. This measurement is an average of four measurements collected using the diameter of the sample as the sound path in the velocity equation. Each measurement location was separated by 45°. These results are given by Table 3.4. Sample 4A, 4C, 4E, and 4G do not have SAW velocity results. The SAW wave mode attenuates more quickly than longitudinal or transverse waves and the sound path is longer across the diameter of the sample than through the thickness so these highly attenuative samples were unlikely to get a reading when measuring the SAW velocity. The results that were collected still have a high standard deviation. This could be due to the positioning of the sample relative to the two transducers used to make the ultrasonic measurement, possible variability in selecting the peak in the waveform for making the measurement or material texture.

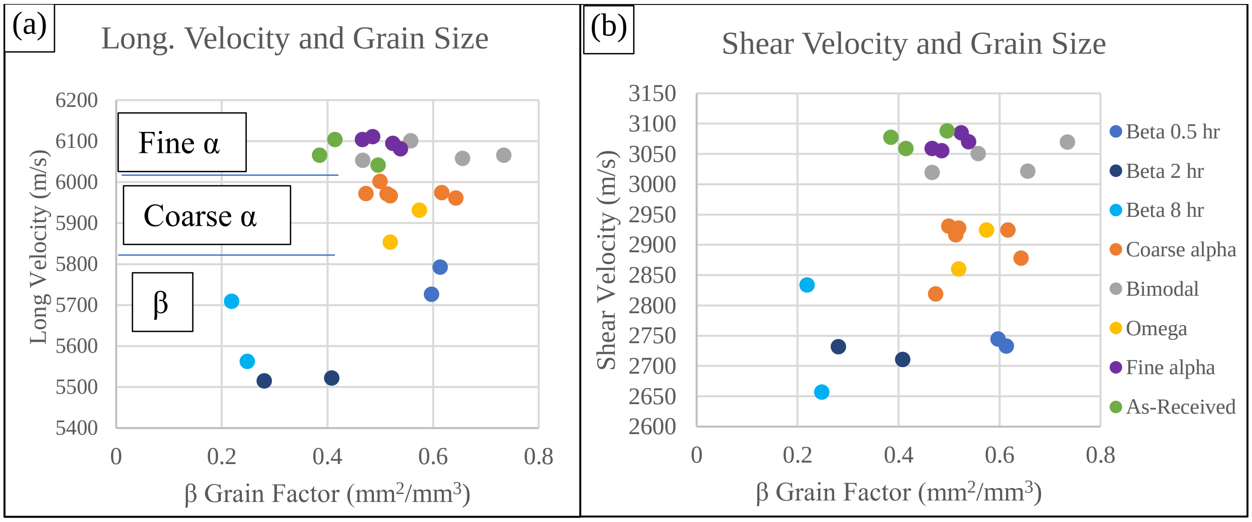

Figure 3.7: Longitudinal and shear ultrasonic velocity compared to β grain size factor.

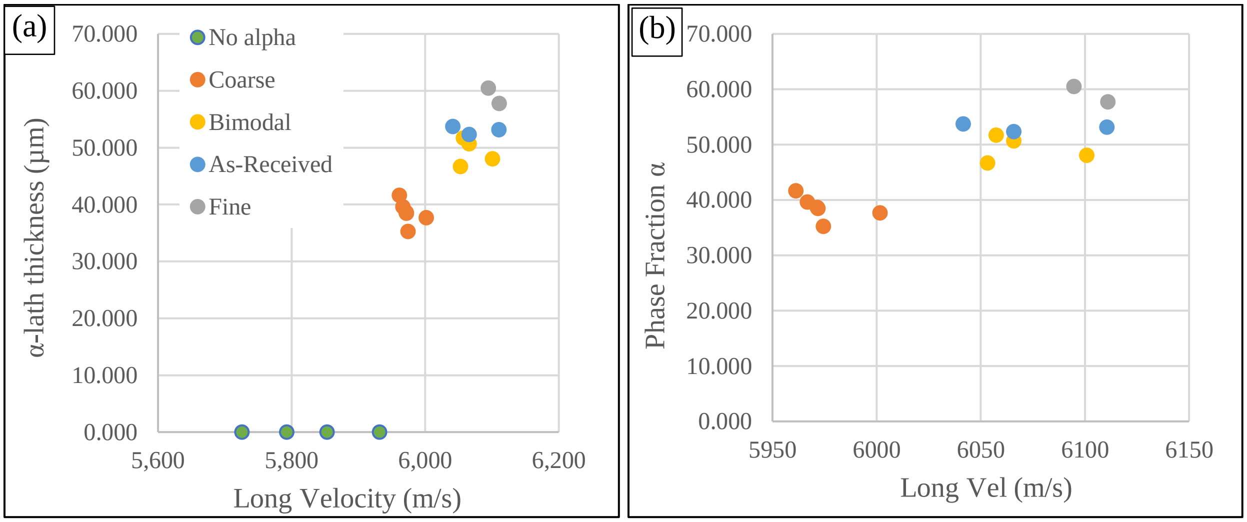

Figure 3.8. Longitudinal velocity compared to α (a) lath thickness and (b) phase fraction.

Table 3.4. The individual and average SAW velocities experimentally measured using contact ultrasonic transducers.

Sample ID (X2)	Heat Treatment	V-0° (m/s)	V-45° (m/s)	V-90° (m/s)	V-135° (m/s)	Average	St Dev
1A	900WQ	2218.6	2259.0	2217.4	2246.2	2235.3	17.9
2A	900WQ	2257.1	2255.8	2243.1	2315.0	2267.8	27.8
1B	900SQ,700-4WQ, 700-4WQ	2798.2	2731.7	2751.6	2751.6	2758.3	24.4
2B	900SQ,700-4WQ, 700-4WQ	2779.1	2808.6	2801.1	2728.9	2779.4	31.1
1C	900WQ, 350-4WQ, 700-4WQ	2721.9	2743.1	2743.1	2759.7	2741.9	13.4
2C	900WQ, 350-4WQ, 700-4WQ	2728.9	2667.0	2719.6	2629.5	2686.2	40.4
1D	900SQ, 700-8FC	2974.3	2963.2	2985.5	2991.1	2978.6	10.7
2D	900SQ, 700-8FC	2991.1	2930.4	2957.7	2991.1	2967.6	25.4
1E	900WQ, 350-4WQ	2471.8	2479.6	2462.3	2404.5	2454.5	29.6
2E	900WQ, 350-4WQ	2458.4	*	2460.3	*	2459.4	0.9
1F	900SQ,550-8WQ	2866.9	2957.7	2919.6	2908.9	2913.3	32.3
2F	900SQ,550-8WQ	2757.3	2781.5	2831.1	2801.1	2792.8	27.0
3B	900SQ, 700-4WQ,550-4WQ	2930.4	2882.5	2900.9	2851.5	2891.3	28.7
3F	900SQ, 700-4WQ,550-4WQ	2841.2	2779.1	2906.3	2866.9	2848.4	46.2
3A	900SQ, 350-4WQ,550-4WQ	2919.6	2914.3	2898.3	2877.3	2902.4	16.5
3G	900SQ, 350-4WQ,550-4WQ	2919.6	2920.7	2916.4	2935.8	2923.1	7.5
3C	900SQ, 700-8WQ	2701.1	2738.3	2728.9	2705.7	2718.5	15.6
3E	900SQ, 700-8WQ	2669.3	2738.3	2728.9	2728.9	2716.4	27.5
R1	NA	2930.4	2903.6	2908.9	2930.4	2918.3	12.2
R2	NA	2925.0	2935.8	2919.6	2935.8	2929.1	7.0
R3	NA	2872.1	2946.7	2887.8	2893.0	2899.9	28.1

SRAS

The previous velocity measurements are commonly performed and could easily be adapted to an ultrasonic inspection procedure, but the bulk measurement of velocity can only provide a bulk or averaged perspective on the role of microstructure. The ability for SRAS to measure the velocity of individual grains can not only provide a large scale and faster measurement of texture than EBSD with less surface prep, but it additionally allows for a better understanding of how microscale velocity relates to the bulk velocity measurements. Figure 3.8 illustrates a clear difference between types of microstructures. The β-phase sample imaging reveals clearly defined beta grains with large velocity differences attributable to grain orientation. The coarse α sample also reveals this velocity difference from grain to grain with less resolution of individual grain boundaries and qualitatively the appearance of a higher velocity. The bimodal and fine α samples qualitatively appear to have an even higher velocity and the differentiation between β grains is obliterated. An argument could be made that these qualitative differences could be attributed to scanning resolution, but these trends are supported by the bulk velocity measurements and later, the attenuation results.

For a better quantitative comparison to bulk velocity measurements, two approaches were used to compare the SRAS SAW measurements to bulk Rayleigh SAW measurements. A perfect comparison cannot be made since SRAS measures a variety of SAW wave modes and bulk measurements must use a less attenuating wave mode so the SAW wave can travel a greater distance between generation and detection.

The first quantitative approach is to calculate what the Rayleigh SAW velocity should be using the measured longitudinal and shear waves. The second approach is to directly measure the velocity of a Rayleigh SAW wave. To compare these results, to SRAS, the velocity of each pixel in the SAW plots pictured in Figure 3.8 was averaged. Figure 3.9 provides a snapshot of the statistics of each sample measured with SRAS which largely confirms what can be observed visually. The velocity does increase as α lath size and phase fraction increases and the standard deviation decreases. Figure 3.10 provides this comparison in SAW velocity measurements. In spite of SRAS using a variety of SAW wave modes, a positive comparison between average SRAS velocity and theoretically calculated or experimentally measured bulk velocity can be made.

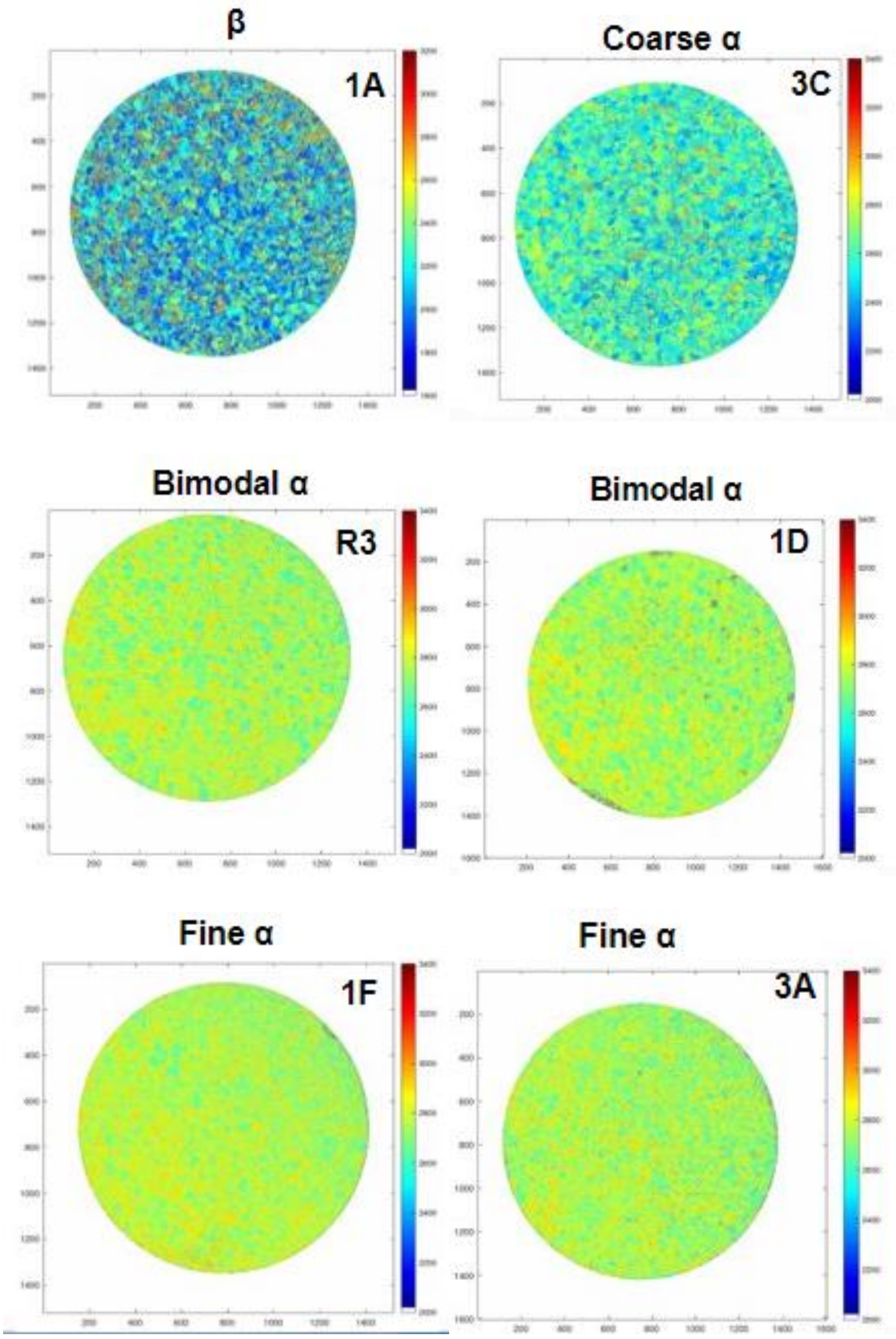

Figure 3.9. SRAS velocity maps of a variety of types of microstructures with velocities given in m/s.

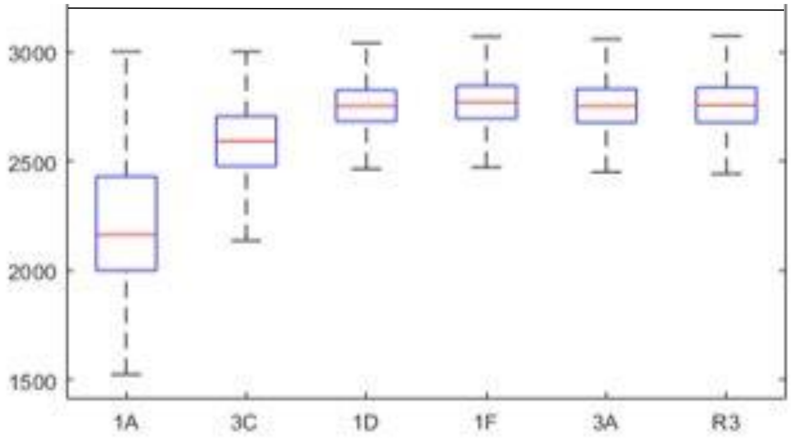

Figure 3.10. Min, max, average, median and standard deviation of each of the SRAS plots from the raw data used to create the plots in Figure 3.8.

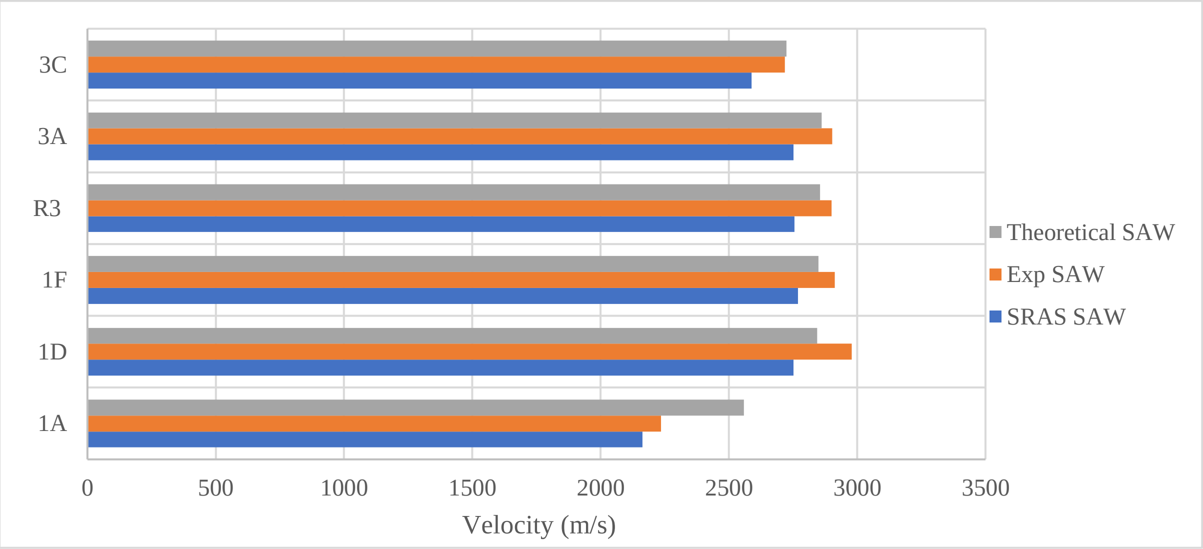

Figure 3.11. Comparison of theoretical SAW velocities calculated using measured long and shear velocity, measured SAW velocity and an average of the SAW velocity raw data.

One of the possible reasons for the deviation between the SRAS and experimental SAW velocity results is the distance measurement used to calculate velocity. It's possible that the transducers were not positioned at the maximum distance corresponding to the diameter of the sample or distance AB in Figure 3.11, but instead, some chord length AB' would be a better representation of the distance traveled by the Rayleigh wave. In the case of sample 1D there is a 7.5% difference between the experimental (or Rayleigh) and SRAS velocities. This deviation in velocity would require a rotation of θ=22.5° to obtain the change in length necessary to account for this velocity difference.

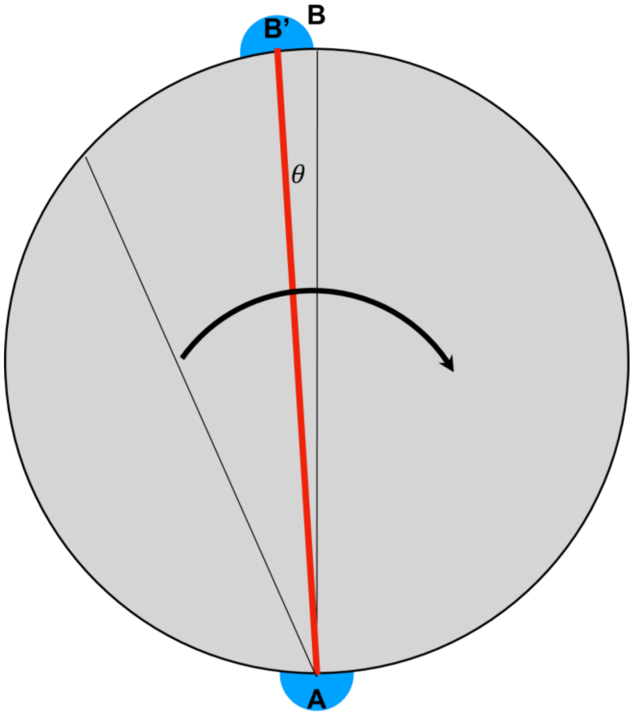

Figure 3.12: the chord between A-B represents the maximum cord distance, while A-B' represents an arbitrary small angle deviation. The example difference for sample 1D would require the more extreme angle to the third, unlabeled cord at 22.5° off the vertical A-B cord, making the hypothesis less than plausible. Thus, other sources of variation should be considered in future work.

Ultrasonic Attenuation

When making velocity measurements, it was immediately apparent that a dramatic attenuation difference occurs between the β, coarse α and samples containing fine α (Figure 3.12). This large difference in attenuation could reasonably be explained when considering the feature size relative to the ultrasonic wavelength. Ultrasonic wavelength can be determined using the equation utilized by SRAS in Chapter 2. Using the longitudinal velocities of these samples presented in the velocity results and the transducer's central frequency of 10 MHz, that would mean the wavelength used to produce the waveform in Figure 3.12 is approximately 0.6 mm. The large β grains being on the order of, or larger than the wavelength cause stochastic scattering which attenuates a significant amount of the ultrasonic energy. The fine α, bimodal and as-received samples contain a high phase fraction of the α phase with α laths small enough to be in the Rayleigh scattering zone. In addition, the SRAS results provide evidence that this high phase fraction of α appears to obliterate the contribution of prior β grain boundaries to the bulk sample attenuation. The samples containing a lower phase fraction of α consisting of coarse α laths do show an increase in attenuation that could either come from the large α lath size or some remaining scattering effect from the prior β grain boundaries.

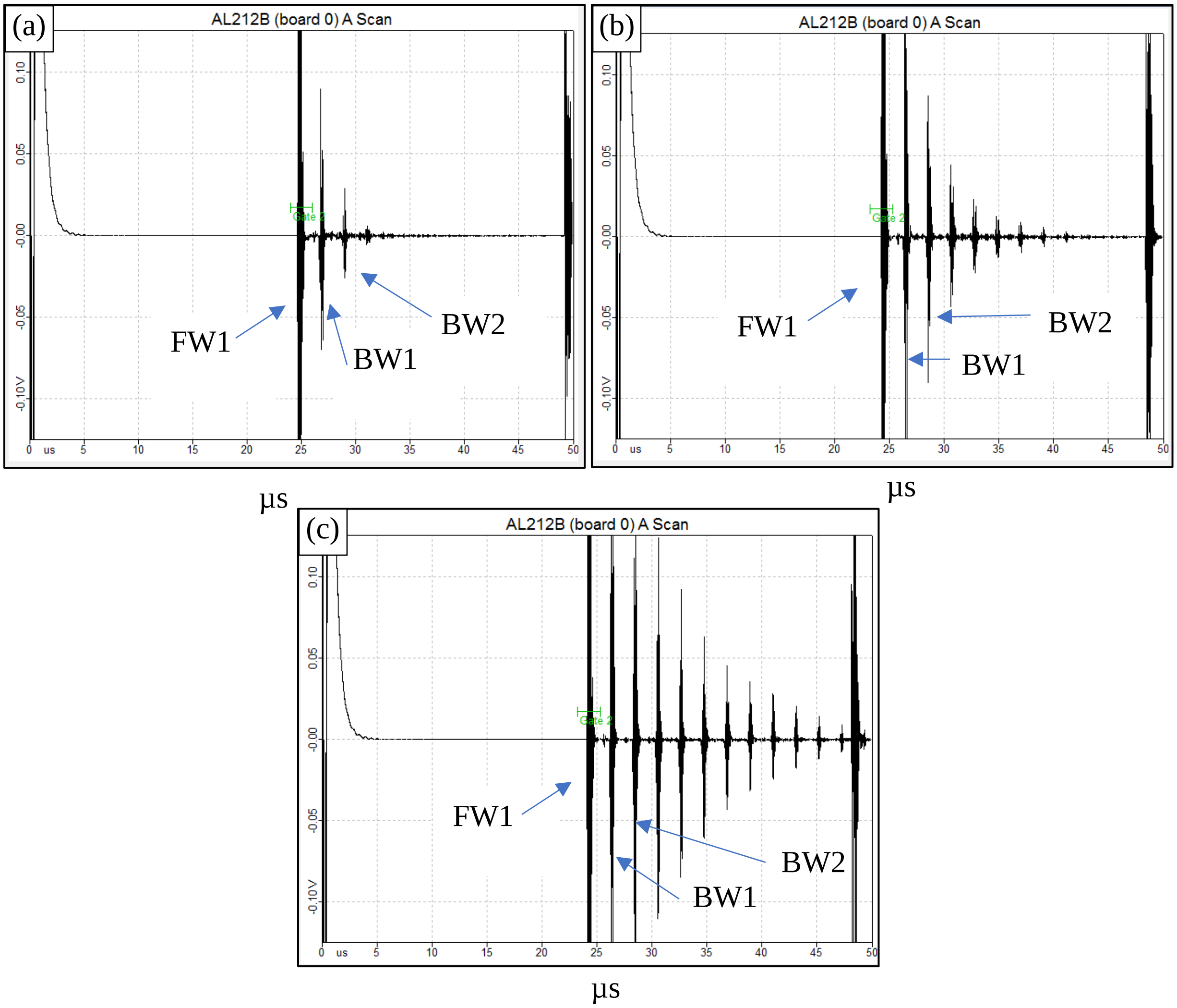

Figure 3.13. Example waveforms captured from a Panametrics 5800 pulser/receiver used for immersion waveform collection. Each waveform was captured using the same 10 MHz unfocused transducer with 20 dB of instrument gain. These waveforms capture a representative signal from (a) the β sample 1A, (b) the coarse α sample 2B and (c) the bimodal sample 2D.

For each sample, FW1, BW1, BW2, and FW2 were captured to calculate the attenuation power law curves as was described previously. These curves give a representation of the attenuation behavior of the sample over a range of frequencies since attenuation is more pronounced with increasing frequency. Example power law curves for each type of microstructure are represented in Figure 3.13 which shows significantly higher attenuation for the β sample than any of the α containing samples and a less pronounced increase in attenuation for samples with lower phase fraction of α (coarse α). In Figure 3.14, each attenuation curve can be compared directly between samples with similar properties.

In a, samples 1C and 2C are coarse α precipitated from prior ω and the remaining samples were all heated at 700° C for 8 hours. 1C and 2C both have attenuations separable from the remaining samples. In b, the bimodal and as received samples are compared. Samples 1D and 2D were bimodal due to continuous cooling as opposed to the stepped approach to creating the bimodal microstructure. Since 3B and 3F have a microstructure that looks similar to the coarse α microstructure but with fine α in some of the regions of retained β, the assumption was that these samples would have comparable attenuation to the coarse α samples. This assumption appears to be incorrect. Another consideration when comparing these bimodal heat treatments is the dispersion of α in the β matrix and the amount of each type. While this parameter was not explicitly measured, there does appear to be a greater quantity of fine α in the microstructure step quenched from 700° C to 550°C since Ti-5553 was allowed to dwell at an optimized temperature for each type of α. This attenuation result indicates that perhaps the quantity of fine α has a bigger impact on attenuation than the phase fraction of α in the β matrix.

Moving on to Figure 3.14.c, sample 3A appears to be an outlier from the remaining fine α samples, approaching an attenuation curve that has some presence of coarse α. It may be true that this sample has some amount of coarse α that was not captured with SEM, or this sample could be a good reminder that the small number of samples and measurements for each microstructure are not sufficient to establish statistical significance. Lastly, d facilitates the discussion of the effect of the isothermal ω phase and the effect of grain size. Samples 1E and 2E containing isothermal ω are indiscernible from the β samples indicating that ω cannot be detected with attenuation, an expected result since TEM is required to verify the presence of ω. The correlation between grain size and attenuation was more difficult to analyze. This should be the most obvious trend since attenuation is supposed to depend on grain size most strongly. These attenuation results do not show clear correlations or trends for a couple reasons that require further investigation. First, samples 4E and 4G do not fit a power law curve. This data, better fits a linear trendline and this method for analyzing attenuation relies on the assumption that the data will have a power law fit. Second, sample 4G had β grain factors and velocities indicating that the heat treatment had not been successful in creating larger grains than the previous β samples.

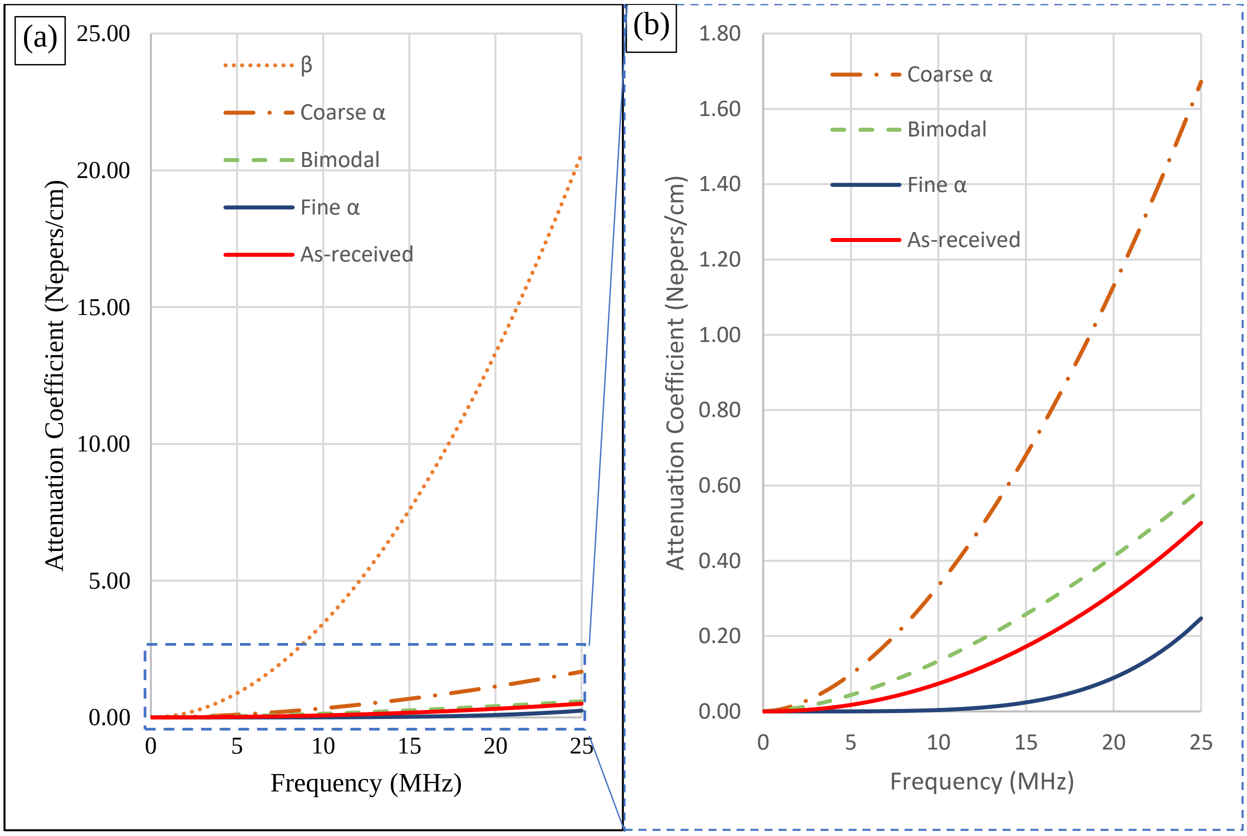

Figure 3.14. Attenuation power law plots. Figure (a) shows curves for each type of microstructure and (b) excluding the β microstructure for better resolution of the differences in samples containing α.

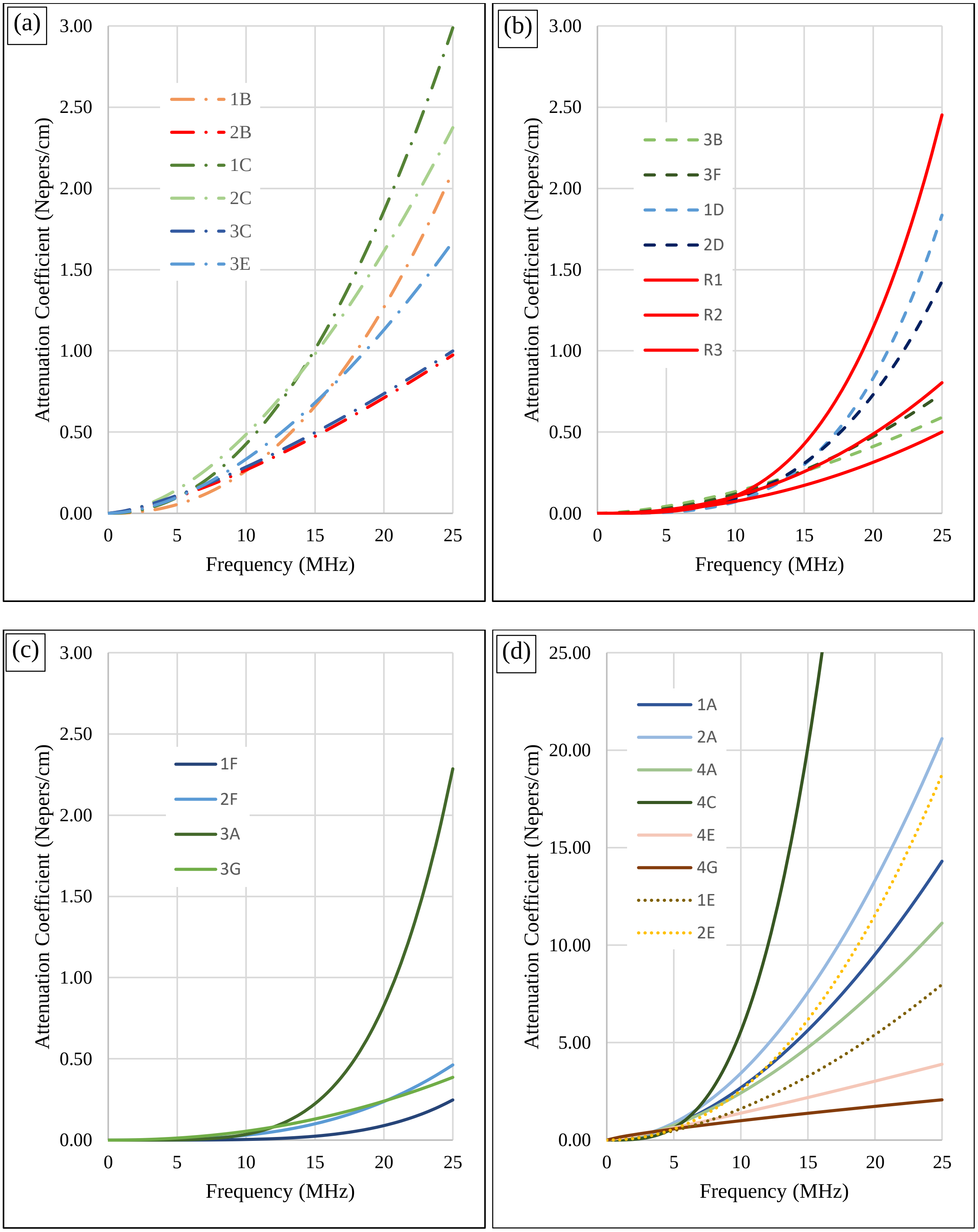

Figure 3.15. Power law curves representing the attenuation of each sample organized by (a) coarse α, (b) bimodal and as-received, (c) fine α, and (d) no α.

In order to gauge the effect of the attenuation to the previously measured material properties, comparisons to the power law exponent and constant were considered. Ultimately, the power law constant was selected for comparisons to microstructural features because it displayed a better correlation. These comparisons are made in Figure 3.15. Here phase fraction of α and α lath thickness both indicate a correlation showing that this measurement technique would justify further investigation.

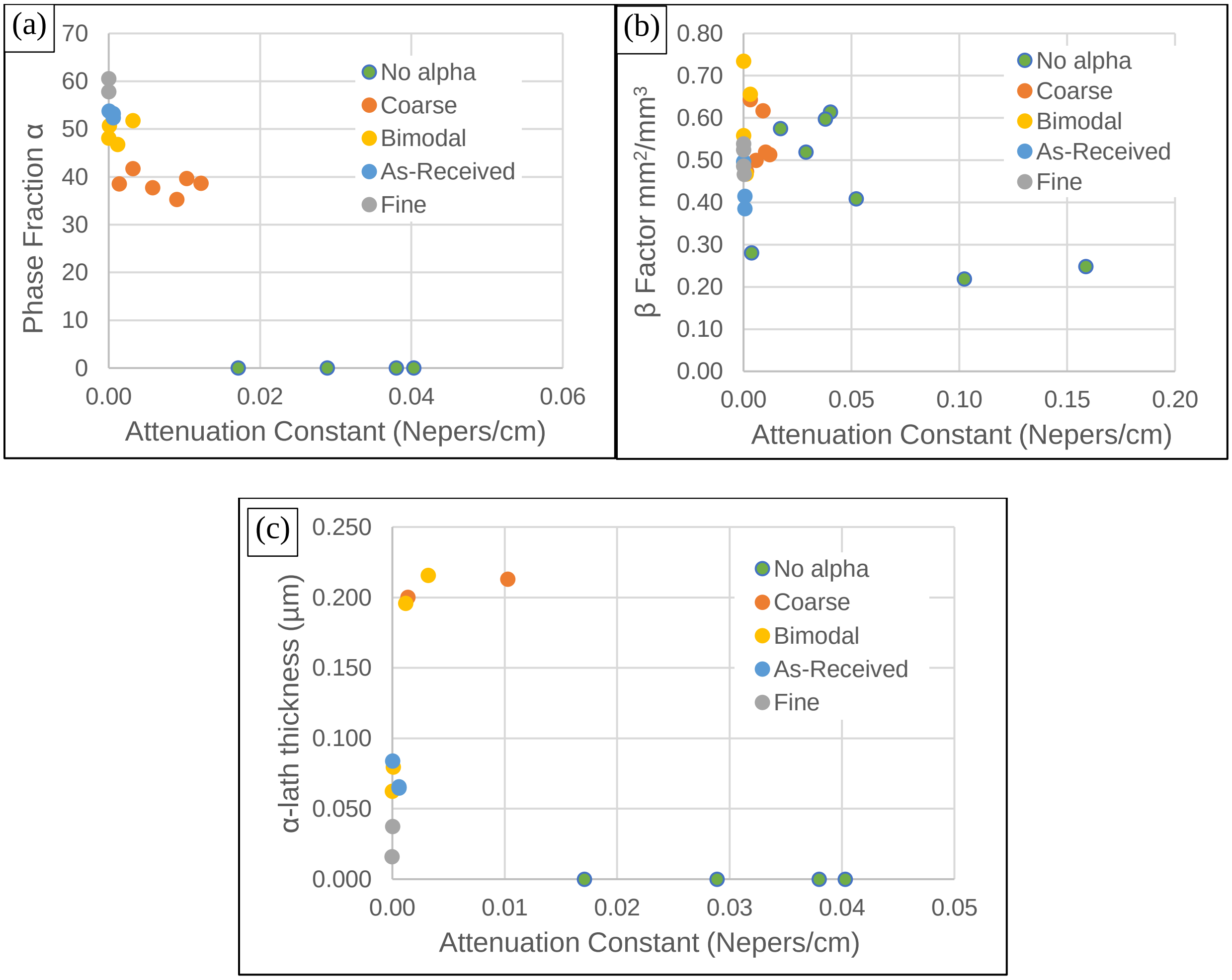

Figure 3.16. Attenuation constant from power law equations is used to compare attenuation to (a) the phase fraction of α, (b) the β grain size, and (c) the α lath thickness.

Mechanical Properties

Mechanical property measurements were made to confirm the microstructural and ultrasonic characterization. These tests included measurements of Vickers hardness and yield stress through cyclic indentation as well as a confirmation of Young’s modulus through nano indentation.

Hardness and Cyclic Indentation

Hardness testing was performed on a β, coarse α, bimodal, fine α and prior ω fine α sample. Each sample was indented with a grid of 25 indents. Samples 1A, 1B, and 2F each had one outlier removed from the data set. As expected, the β sample 1A had the lowest hardness and the fine α sample 3A had the highest hardness. The same machine with a ball indenter tip was used to generate cyclic indentation curves in order to calculate the yield stress of the pairs of the samples used for hardness testing except for 3A which was polished and indented for each measurement.

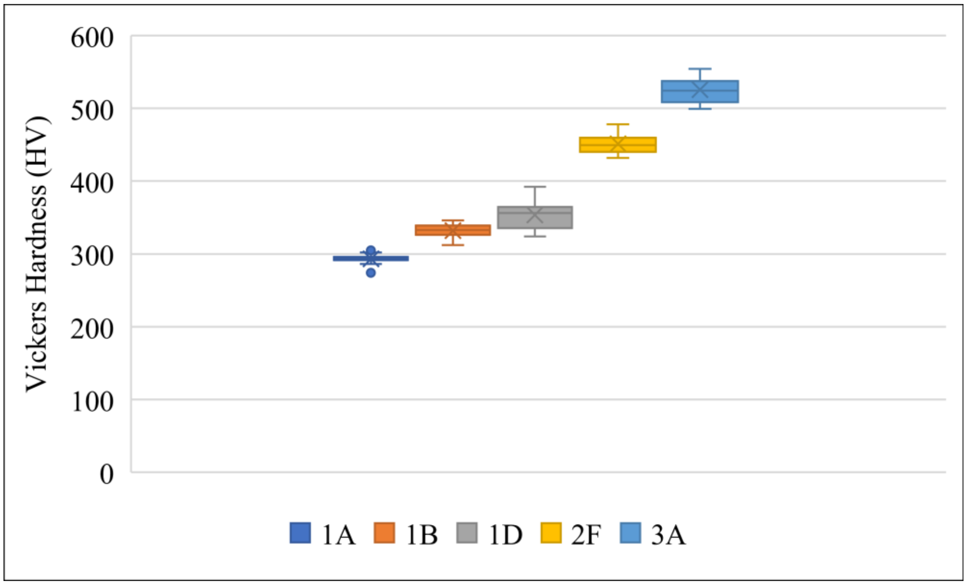

Figure 3.17. Hardness testing results with outliers removed.

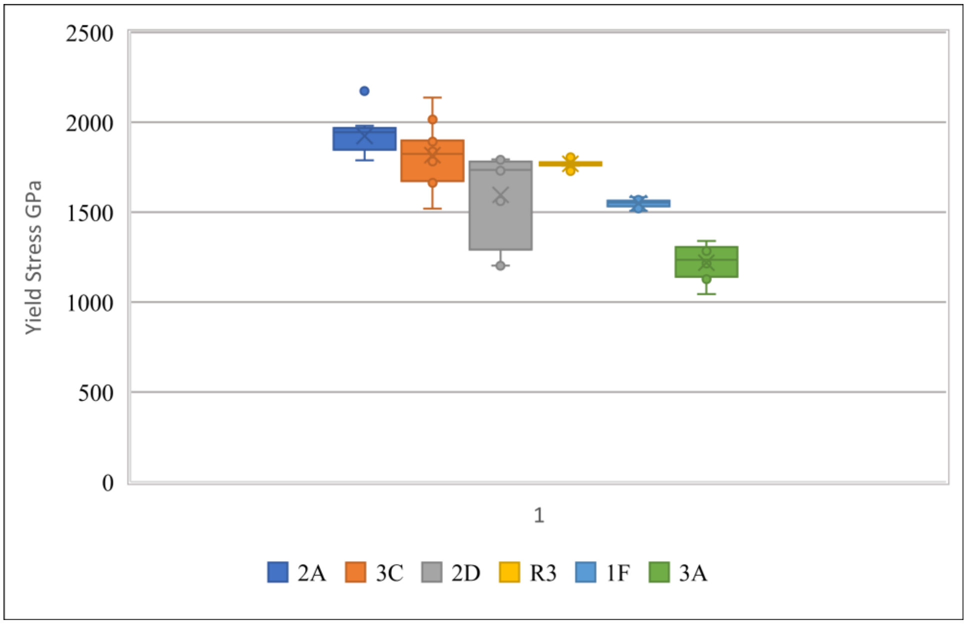

Figure 3.18. Average and standard deviation from cyclic testing.

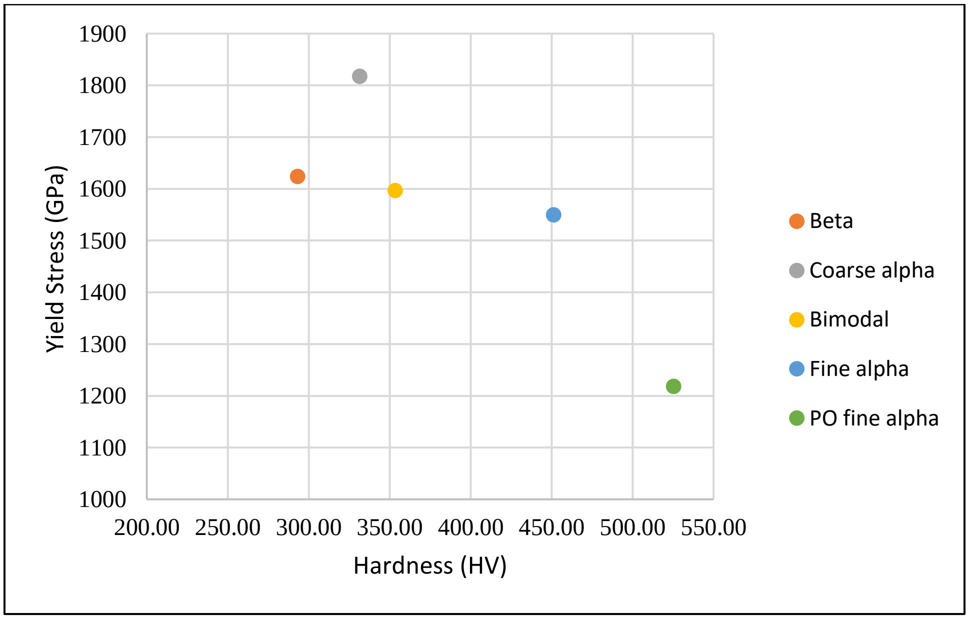

Figure 3.19. Hardness compared to yield stress from cyclic indentation.

Since cyclic indentation is a relatively new method for getting stress, it is difficult to compare these values directly to tensile or compression results from the literature. In a study from Suryawanshi, tensile and compression stress strain curves were generated for several materials including Ti-5553 with a β microstructure and α-β microstructure [48]. This study shows that Ti-5553 has a pronounced tension-compression asymmetry which may, in part account for the differences between the yield stress values collected for this study.

Nano Indentation

A set of 20 Berkovich nanoindentations were made with an indentation depth of 500 nanometers. At this depth, both α and β phases were measured on coarse α sample 3E. These indents measured an average Young’s modulus of 108.8 GPa +/- 7/8 GPa and an average Berkovich hardness of 3.5 GPa +/- 0.5 GPa. The modulus calculated using ultrasonic velocity is 107.1 GPa, a 1.5% difference. When considering the variation in velocity revealed by SRAS, the fact that the ultrasonic velocity averages many grains and the nano indent interacts with only a few α laths on the sample surface, a 1.5% difference in modulus, shows a promising agreement with the ultrasonic data, but not enough data is collected here to definitely prove a correlation.

CHAPTER 4. CONCLUSIONS AND RELEVANCE

Conclusions

Ti-5553 is an interesting material for its microstructural variation which is relatively simple to obtain. Of the 25 heat treatments executed in this study only one sample 4G may not have transformed into the intended microstructure. In addition, this metastable β alloy demonstrates that caution should be taken when assuming homogeneous ultrasonic elastic properties. This was only a proof of concept in the use of ultrasonic inspection techniques for characterizing changes in Ti-5553 microstructures, but it was demonstrated that at a minimum, significant alterations to the heating parameters of this alloy will result in differences in measured attenuation, velocity, hardness and yield stress. The comparison between the surface velocities measured with SRAS and conventional techniques aids in the understanding of how sound interacts with both α and β phases in this alloy with a potential for application to other titanium alloys.

In particular, the phenomenon where coarse α precipitating from grain boundaries being differentiable from coarse α precipitating from prior ω and the obliteration of prior β grain boundaries with fine α precipitation resulting in a material with nearly no attenuation in normal ultrasonic operating frequency ranges would be interesting phenomena for future study. In order to determine if smaller variations in microstructure can reliably be detected, more samples should be heated in a narrower temperature range with enough ultrasonic measurements to establish statistical significance.

Relevance

β-stabilized Ti samples provide an interesting opportunity to explore the ultrasonic velocity and attenuation responses to individual phases. The discovery of the large differences in ultrasonic attenuation between samples was unexpected and may open up some opportunities for using this or a similar attenuation measurement technique to identify deleterious microstructures in Ti-5553 due to improper aging or unexpected thermal cycling. These dramatically large differences in attenuation and even velocity should be considered when designing flaw detection-based inspection plans for samples made of Ti-5553. Many flaw detection techniques make judgements of the acceptability of detected indications based on amplitude. This very common assumption would mean that significant changes in amplitude due to microstructural changes could result in false positive or false negative results. A proposition that could have significant consequences in terms of safety and reliability, the cornerstones of the NDE field.

These results could also be expanded to create more accurate models of not only Ti-5553 but these findings may be able to improve models of other β-stabilized or α-β stabilized titanium alloys, as well as heat-treatable alloys in general. Ultrasonic wave propagation has been studied in many contexts for many years, but this study demonstrates that there is still more that can be learned about this physical phenomenon and there is more that ultrasound can teach about material science. Of immediate relevance and future direction is the need to address multi-phase materials consisting of variants of precipitates that have anisotropic elastic properties, and to predict how the elastic properties of the polycrystalline, two-phase material changes as the precipitates form and the composition (and thus elastic properties) of the matrix phase evolve.

REFERENCES

[1] Crocker, M., 1997, *Encyclopedia of Acoustics*, John Wiley & Sons, Inc., Hoboken, NJ, USA.

[2] Moore, P., Workman, G., and Kishoni, D., eds., 2007, *Nondestructive Testing Handbook*, American Society of Nondestructive Testing, Columbus.

[3] Quintana, M., Ji, Y., and Collins, P., 2022, "A Perspective of The Needs and Opportunities for Coupling Materials Science and Nondestructive Evaluation for Metals-Based Additive Manufacturing," Mater Eval, **80**(4), pp. 45–63.

[4] Schroeder, C. J., Conner, R. J., Crowley, B. M., and Washer, G. A., 2021, "Acoustic Properties of Steel Bridge Base Metals," Research in Nondestructive Evaluation, **32**(5), pp. 238–262.

[5] Russell, A. M., and Lee, K. L., *STRUCTURE-PROPERTY RELATIONS IN NONFERROUS METALS*.

[6] Lutjering, G., and Williams, J. C., 2007, *Titanium - 2nd Edition*.

[7] Cotton, J. D., Boyer, R. R., Briggs, R. D., Baggerly, R. G., Meyer, C. A., Carter, M. D., Wood, W., Tewksbury, G., Li, V., and Yao, X., 2007, "Phase Transformations in Ti-5Al-5Mo-5V-3Cr-0.5Fe," *11th World Conference on Titanium (JIMICS) at Kyoto, Japan*, Proceedings of the 11th World Conference on Titanium (JIMIC5), Kyoto.

[8] Temple, A. J., Lesar, R. A., Johnson, D. D., Thuo, M. M., and Leifsson, L. T., *Mechanical Properties of Heat-Treated Additively Manufactured Titanium Alloys*.

[9] Clement, N., 2010, *UNIVERSITE CATHOLIQUE DE LOUVAIN Louvain-La-Neuve Phase Transformations and Mechanical Properties of the Ti-5553 β-Metastable Titanium Alloy Composition Du Jury*.

[10] Cotton, J. D., Briggs, R. D., Boyer, R. R., Tamirisakandala, S., Russo, P., Shchetnikov, N., and Fanning, J. C., 2015, "State of the Art in Beta Titanium Alloys for Airframe Applications," JOM, **67**(6), pp. 1281–1303.

[11] Sinklert, W., and Luzzi, D. E., 1994, *AN ELECTRON DIFFRACTION INVESTIGATION OF THE DIFFUSE O~ STRUCTURE IN QUENCHED Ti-3d TRANSITION METAL ALLOYS*.

[12] Nag, S., Banerjee, R., Srinivasan, R., Hwang, J. Y., Harper, M., and Fraser, H. L., 2009, "ω-Assisted Nucleation and Growth of α Precipitates in the Ti-5Al-5Mo-5V-3Cr-0.5Fe β Titanium Alloy," Acta Mater, **57**(7), pp. 2136–2147.

[13] Contrepois, Q., Carton, M., and Lecomte-Beckers, J., 2011, "Characterization of the β Phase Decomposition in Ti-5Al-5Mo-5V-3Cr at Slow Heating Rates," Open J Met, **01**(01), pp. 1–11.

[14] Carlton, H. D., Klein, K. D., and Elmer, J. W., 2019, "Evolution of Microstructure and Mechanical Properties of Selective Laser Melted Ti-5Al-5V-5Mo-3Cr after Heat Treatments," Science and Technology of Welding and Joining, **24**(5), pp. 465–473.

[15] Foltz, J., Williams, J., Fraser, H., and Katharine, F., "The Relationship Between Microstructure, Tensile Properties and Fatigue Life in Ti-5Al-5V-5Mo-3Cr-0.4Fe (Ti-5553)."

[16] Welk, B. A., Fraser, H. L., and Williams, J. C., *Microstructural and Property Relationships In-Titanium Alloy Ti-5553*.

[17] Wang, W., Zhang, X., Mei, W., and Sun, J., 2020, “Role of Omega Phase Evolution in Plastic Deformation of Twinning-Induced Plasticity β Ti–12V–2Fe–1Al Alloy,” Mater Des, **186**.

[18] Ensminger, Dale., 2012, *Ultrasonics : Fundamentals, Technologies, and Applications,* CRC Press, Boca Raton, FL.

[19] Graff, K. F., 1991, *Wave Motion in Elastic Solids,* Dover.

[20] Herman, H., 1972, *Treatise on Materials Science and Technology,* Academic Press, New York.

[21] Jayakumar, T., and Kumar, A., 2014, “Characterization of Metals through Elastic Properties-Kumar,” Journal of Pure and Applied Ultrasonics, **36**(2–3), pp. 29–35.

[22] Dakota Ultrasonics, 2023, “References: Appendix A Velocity Table.”

[23] Krautkrämer, Josef., 1990, *Ultrasonic Testing of Materials,* Springer-Verlag, Berlin ;

[24] Palani, P., Joseph, A., Jayakumar, T., and Raj, B., 1995, *Ultrasonic Velocity Measure-Ments for Estimation of Grain Size in Austenitic Stainless Steel*.

[25] Hirao, M., and Aoki, K., 1987, “Texture of Polycrystalline Metals Characterized by Ultrasonic Velocity Measurements,” Journal of the Acoustical Society of America, **81**(5), pp. 1434–1440.

[26] Sayers, C. M., 1982, *Ultrasonic Velocities in Anisotropic Polycrystalline Aggregates*.

[27] Smith, R. J., Li, W., Coulson, J., Clark, M., Somekh, M. G., and Sharples, S. D., 2014, “Spatially Resolved Acoustic Spectroscopy for Rapid Imaging of Material Microstructure and Grain Orientation,” Meas Sci Technol, **25**(5).

[28] Bai, X., Zhao, Y., Ma, J., Liu, Y., and Wang, Q., 2018, “Grain-Size Distribution Effects on the Attenuation of Laser-Generated Ultrasound in α-Titanium Alloy,” Materials, **12**(1).

[29] Papadakis, E. P., 1965, “Ultrasonic Attenuation Caused by Scattering in Polycrystalline Metals,” J Acoust Soc Am, **37**(4), pp. 711–717.

[30] Stanke, F. E., and Kino, G. S., 1984, “A Unified Theory for Elastic Wave Propagation in Polycrystalline Materials,” Journal of the Acoustical Society of America, **75**(3), pp. 665–681.

[31] Weaver, R. L., 1990, *DIFFUSIVITY OF ULTRASOUND IN POLYCRYSTALS*.

[32] Kube, C. M., and Arguelles, A. P., 2016, “Bounds and Self-Consistent Estimates of the Elastic Constants of Polycrystals,” Comput Geosci, **95**, pp. 118–122.

[33] Arguelles, A. P., and Turner, J. A., 2017, “Ultrasonic Attenuation of Polycrystalline Materials with a Distribution of Grain Sizes,” J Acoust Soc Am, **141**(6), pp. 4347–4353.

[34] Li, A., 2003, “Study of the Effect of Microstructure on Ultrasonic Signal Attenuation,” AIP Publishing, pp. 1322–1329.

[35] Van Pamel, A., Sha, G., Lowe, M. J. S., and Rokhlin, S. I., 2018, “Numerical and Analytic Modelling of Elastodynamic Scattering within Polycrystalline Materials,” J Acoust Soc Am, **143**(4), pp. 2394–2408.

[36] Sha, G., Huang, M., Lowe, M. J. S., and Rokhlin, S. I., 2020, “Attenuation and Velocity of Elastic Waves in Polycrystals with Generally Anisotropic Grains: Analytic and Numerical Modeling,” J Acoust Soc Am, **147**(4), pp. 2442–2465.

[37] Bhattacharjee, A., Pilchak, A. L., Lobkis, O. I., Foltz, J. W., Rokhlin, S. I., and Williams, J. C., 2011, “Correlating Ultrasonic Attenuation and Microtexture in a Near-Alpha Titanium Alloy,” Metall Mater Trans A Phys Metall Mater Sci, **42**(8), pp. 2358–2372.

[38] Zhang, X.-G., Simpson, W. A., Vitek, J. M., Barnard, D. J., Tweed, L. J., and Foley, J., 2004, "Ultrasonic Attenuation Due to Grain Boundary Scattering in Copper and Copper-Aluminum," J Acoust Soc Am, **116**(1), pp. 109–116.

[39] Viswanath, A., Kumar, A., Jayakumar, T., and Purnachandra Rao, B., 2015, "Ultrasonic Characterization of Microstructural Changes in Ti-10V-4.5Fe-1.5Al β-Titanium Alloy," Metallurgical and Materials Transactions A, **46**(8), pp. 3393–3405.

[40] Searles, T., Tiley, J., Tanner, A., Williams, R., Rollins, B., Lee, E., Kar, S., Banerjee, R., and Fraser, H. L., 2005, "Rapid Characterization of Titanium Microstructural Features for Specific Modelling of Mechanical Properties," Meas Sci Technol, **16**(1), pp. 60–69.

[41] Kar, S. K., Ghosh, A., Fulzele, N., and Bhattacharjee, A., 2013, "Quantitative Microstructural Characterization of a near Beta Ti Alloy, Ti-5553 under Different Processing Conditions," Mater Charact, **81**, pp. 37–48.

[42] Russ, J. C., and Dehoff, R. T., 2000, *Practical Stereology*, Springer US, Boston, MA.

[43] Rogers, P. H., and Van Buren, A. L., 1974, "An Exact Expression for the Lommel-diffraction Correction Integral," J Acoust Soc Am, **55**(4), pp. 724–728.

[44] Margetan, F. J., Panetta, P. D., and Thompson, R. B., *ULTRASONIC SIGNAL ATTENUATION IN ENGINE TITANIUM ALLOYS*.

[45] Panetta, P. D., Margetan, F. J., Yalda, I., and Thompson, R. B., 1996, "Ultrasonic Attenuation Measurements in Jet-Engine Titanium Alloys," Review of Progress in Quantitative Nondestructive Evaluation, pp. 1525–1532.

[46] Li, W., Coulson, J., Aveson, J. W., Smith, R. J., Clark, M., Somekh, M. G., and Sharples, S. D., *Orientation Characterisation of Aerospace Materials by Spatially Resolved Acoustic Spectroscopy*.

[47] Weaver, J. S., Khosravani, A., Castillo, A., and Kalidindi, S. R., 2016, "High Throughput Exploration of Process-Property Linkages in Al-6061 Using Instrumented Spherical Microindentation and Microstructurally Graded Samples," Integr Mater Manuf Innov, **5**(1), pp. 192–211.

[48] Suryawanshi, J., Singh, G., Msolli, S., Jhon, M. H., and Ramamurty, U., 2021, "Tension-Compression Asymmetry and Shear Strength of Titanium Alloys," Acta Mater, **221**.